Nonlinear Equilibration of Thermohaline Intrusions

DAVID WALSH AND BARRY RUDDICK

Department of Oceanography, Dalhousie University, Halifax, Nova Scotia, Canada

(Manuscript received 29 October 1996, in final form 13 August 1997)

ABSTRACT

The nonlinear behavior of thermohaline intrusions on a wide front is investigated using a one-dimensional numerical model. The model is used to follow the evolution of a field of intrusions from infinitesimal amplitude to a large-amplitude state characterized by inversions in temperature and salinity. It is thus possible to extend the analytical studies of Toole and Georgi and others to large amplitude, allowing for the effects of amplitude-dependent diffusivities, and for the appearance of stably stratified, diffusively stratified, and statically unstable regions in the water column as the intrusions grow.

The model runs are initialized with infinitesimal disturbances that grow exponentially in time until inversions in temperature and salinity occur. After inversions appear, the intrusions evolve toward an equilibrium state in which friction balances buoyancy forces, for both finger- and diffusive-sense basic-state stratifications. These equilibrium states are characterized by statically unstable ''convecting'' layers between layers of finger- and diffusively stratified fluid—the convecting layers appear when intrusions reach large amplitude and help to slow their growth. Equilibration seems to be insensitive to the specific functional forms chosen for the double-diffusive diffusivities and viscosities. The necessary condition for equilibration is that the *T–S* flux ratio adjusts as the intrusions grow, and (within the context of the present model) turbulent mixing provides the mechanism for this adjustment.

1. Introduction

Quasi-lateral thermohaline interleaving is often observed in areas of the ocean where waters with different *T–S* properties meet laterally. First documented by Stommel and Fedorov (1967), interleaving has since been observed in fronts and on mesoscale eddies by many other researchers (Joyce et al. 1978; Horne 1978; Toole 1981; Barton and Hughes 1982; Ruddick and Hebert 1988; Provost and Gana 1995). Recently, Carmack et al. (1995) have observed interleaving on a grand scale in the Arctic Ocean, finding intrusions coherent over horizontal scales of more than 2000 km. Richards and Pollard (1991) have documented intrusions in the equatorial Pacific that can be traced for up to 400 km, which they speculate may be an important mechanism for mixing salty water from south of the equator with fresher northern water.

Because interleaving is associated with the advection of tongues of water across a front, it could provide an important mechanism for cross-frontal exchange of heat, salt, and momentum. The frequency with which interleaving has been observed suggests that it could play a role in the dynamics of a wide range of features ranging in size from the mesoscale to the basin scale. Based on extrapolations from linear theory, Posmentier and Kirwan (1985) have suggested that double-diffusive interleaving may have an important effect on rings and other mesoscale features, possibly acting to *enhance* their density signatures while running down their *T–S* signatures. Garrett (1982) has suggested that interleaving may provide a link between lateral stirring and diapycnal mixing since stirring by mesoscale eddies can alter frontal *T–S* gradients, which can in turn affect diapycnal intrusive fluxes (by modifying intrusion growth rates).

Unfortunately, due to the extremely small velocities associated with interleaving [$\sim$1 mm s^{-1} according to Ruddick and Hebert (1988)], it has proved extremely difficult to quantify intrusive fluxes in the ocean. In addition, because frontal existence timescales in the ocean are typically much longer than intrusive growth timescales, intrusions spend most of their lives in a large amplitude, nonlinear state; so the usefulness of extrapolating from linear theory is questionable. Hence, as a result of the difficulty of making direct measurements of intrusive velocities and because of the lack of adequate theoretical models, the dynamical importance of interleaving is largely unknown. Bormans (1992) has carried out laboratory experiments simulating intrusions on a ''sharp'' *T–S* front and found an empirical relation that predicts intrusive fluxes well in doubly stable conditions. The implications of these results for oceanic intrusions are, however, unclear. The only direct inference of intrusive fluxes in the ocean is that due to Ruddick and Hebert (1988), who demonstrated that the dominant mechanism responsible for the decay and eventual demise of Meddy Sharon was thermohaline interleaving, presumably driven by double-diffusive buoyancy fluxes. Over the 2-yr period of observation, intrusions at the

Corresponding author address: Dr. David Walsh, Department of Oceanography, Dalhousie University, Halifax, NS B3H 4J1, Canada. E-mail: dwalsh@phys.ocean.dal.ca

edge of the meddy core eroded the warm and salty central region from an initial diameter of ~60 km to less than 5 km, suggesting an effective lateral diffusivity of 2–4 $m^2\ s^{-1}$. These observational results demonstrate that intrusions can have an important effect on the evolution of oceanic fronts and eddies.

Joyce (1977) proposed a model for interleaving at statistical equilibrium, which permits intrusive fluxes to be inferred from *T*–*S* profiles. Joyce assumed that the production of salinity variance by lateral advection is balanced, on average, by dissipation of salinity variance through small-scale vertical mixing. This allows the lateral intrusive fluxes to be expressed in terms of horizontal and vertical salinity gradients and a vertical diffusivity, K_V. Assuming a diffusivity of $10^{-4}\ m^2\ s^{-1}$, Joyce et al. (1978) estimated that intrusions in the Antarctic Circumpolar Front were responsible for an effective lateral diffusivity of $\sim 20\ m^2\ s^{-1}$, roughly equivalent to the eddy-driven fluxes across the front (Bryden 1979). Joyce's model has been applied frequently since its introduction. Provost and Gana (1995) have used it to estimate an effective salt diffusivity of 100 $m^2\ s^{-1}$ due to interleaving at the Brazil–Malvinas confluence, while Richards and Pollard (1991) estimate a remarkably large value of 3000 $m^2\ s^{-1}$ based on their equatorial measurements. A limitation of Joyce's model is that it relies upon prior knowledge of K_V, which is poorly known at this time, particularly in intrusive regions where both double-diffusive and ''ordinary'' turbulent mixing are likely to be occurring.

Stern (1967) suggested that interleaving could arise spontaneously under the action of double-diffusive fluxes in regions with strong lateral *T*–*S* variations. However, the theory he formulated to explain interleaving predicted unbounded growth rates for disturbances of vanishingly small scale (an ''ultraviolet catastrophe'') and, hence, could not explain the finite intrusion scales seen in the ocean. Stern's inviscid theory was modified by Toole and Georgi (1981), who found that adding friction prevented the UV catastrophe from occurring; their theory predicted a finite wavelength for the fastest-growing intrusions, and the predicted length scales were found to be in reasonably good agreement with observations. Since then, numerous analytical studies have appeared in the literature, many of which are variations on the linear stability calculation of Toole and Georgi. For example, McDougall (1985a) incorporated ''slab'' flux laws into Toole and Georgi's model and showed that this could lead to an increase in the vertical scale of the fastest growing intrusion. Niino (1986) investigated the effect of a finite width front on growing intrusions, thus reconciling the ''wide front'' model of Toole and Georgi with the ''narrow front'' model proposed by Ruddick and Turner (1979). Walsh and Ruddick (1995a) examined the influence of density-ratio-dependent diffusivities and viscosity on the growing intrusions, and found that even a weak density ratio dependence can significantly affect growth rates and vertical scales.

Linearized studies such as that of Toole and Georgi (1981) predict intrusion length scales, growth rates, and slopes, but say nothing about the finite-amplitude state or about the fluxes of heat and salt produced by interleaving. The reason for this is that only the initial (exponential growth) phase of the intrusion life cycle is modeled by the linear stability analyses, while the fluxes depend critically on the form of the equilibrium that the growing intrusions eventually reach. McDougall (1985b) extended the existing linear stability analyses, investigating the possibility of equilibrium interleaving solutions that might occur when exponentially growing small amplitude solutions grow to large amplitude. His results suggest that, if the water column is initially stratified in the salt-finger sense, growing intrusions will eventually produce *T*–*S* inversions and, hence, diffusively stratified regions. Equilibration of growing intrusions is then possible via a three-way balance (in *T*–*S* space) between finger, diffusive, and advective *T*–*S* fluxes. The essential factor is that these processes have different *T*–*S* flux ratios, making it possible to achieve an equilibrium *T*–*S* flux balance. While McDougall established a necessary condition for equilibrium, he did not demonstrate that small amplitude solutions can ever actually evolve to the large amplitude equilibrium states he discusses. McDougall performed a heuristic stability analysis that suggested that, if such solutions could be achieved, they should be stable. However, Kerr (1992) has shown analytically that large amplitude, marginally stable (i.e., nongrowing) intrusions may be unstable to smaller-scale double-diffusive instabilities, suggesting that equilibrium interleaving solutions may be unstable.

In an analysis of the evolution of a horizontal thermohaline intrusion bounded by diffusive and finger interfaces above and below, Ruddick (1984) found that the diffusivity formulations had to be of a special form to allow equilibrium solutions. He chose diffusivities that were functions of the interfacial density ratio ($=\alpha\Delta T/\beta\Delta S$) and found that to achieve an equilibrium it was necessary that the diffusive-sense diffusivity vary more rapidly (as a function of density ratio) than the finger-sense diffusivity. This allowed finger buoyancy fluxes to dominate at moderate or large density ratios, with diffusive buoyancy fluxes dominating at small values of R_ρ. It should be noted that Ruddick's study focused on the evolution of horizontal intrusions with no lateral advection, whereas lateral advection is likely to be important to the dynamics of oceanic intrusions.

Apart from the aforementioned studies by McDougall (1985b), Ruddick (1984), and Kerr (1992), the question of whether equilibrium interleaving solutions exist and are achievable is largely unaddressed. The studies of Ruddick and McDougall suggest that both the appearance of diffusive interfaces and the specific functional

forms of the diffusivities may be important in the equilibration of growing intrusions.

Our primary goal in the present work is to show that the incorporation of amplitude-dependent mixing coefficients and ''background'' turbulence in Toole and Georgi's model allows growing intrusions to equilibrate at large amplitude (after *T*–*S* inversions appear). To this end, we have developed a simple one-dimensional numerical model of thermohaline interleaving, and will present a series of model runs to demonstrate that evolving intrusions can approach a steady-state configuration under meddylike conditions. These equilibria are reached through the evolution of small amplitude intrusions to large amplitude, and they are found to be in reasonably good agreement with the intrusion data from Meddy Sharon. We then attempt to identify and understand the mechanisms necessary for equilibration. A detailed consideration of the dependence of intrusive fluxes on model parameters and of the stability of the solutions will be the topic of a future manuscript.

The outline of the paper is as follows: we begin by describing and validating the numerical model (section 2) and then use it to look at the evolution of small amplitude intrusions to large amplitude (section 3). In section 4 we demonstrate that growing intrusions approach an equilibrium state under conditions similar to those found in Meddy Sharon and discuss the factors that allow equilibration. In section 4 we also explore the sensitivity of the model solutions to background mixing, the sense of the overall stratification, and to the functional forms chosen for the diffusivities and viscosity. We end with a discussion section (section 5) and conclusions (section 6).

2. The model

Walsh and Ruddick (1995a) demonstrated that the slope and wavelength of the intrusions in Meddy Sharon were in good agreement with the predictions of linear theory in both the lower (finger stratified) and upper (diffusively stratified) halves of the meddy. They inferred that the slope and wavenumber set by the linear instability mechanism remain fixed as intrusions grow to a large amplitude state characterized by inversions in the temperature and salinity fields. Based on this observational result, we have constructed a one-dimensional numerical model to investigate the large amplitude behavior of intrusions. The resulting model contains much of the relevant physics, executes rapidly, and allows an investigation of the nature of the equilibria reached by growing intrusions. Our fundamental assumption is that intrusions are planar disturbances on a ''wide'' front and, hence, are not seriously affected by end effects. It is also implicitly assumed that the linear growth timescale for the intrusions is much less than the ''frontal existence'' timescale, so the basic state can be considered to be invariant on intrusive timescales.

In addition to fixing the slope and wavelength of the intrusions, a number of assumptions are made concerning the various small-scale mixing processes driving the intrusions. Both double-diffusive fluxes and turbulent fluxes are parameterized using conventional eddy diffusivities and viscosities. When conditions are double-diffusively unstable, diffusivities are taken to be functions of the density ratio (R_ρ), defined as

$$R_\rho = \frac{\alpha T_z}{\beta S_z}, \tag{1}$$

which measures the relative contributions of *T* and *S* to the density stratification. Walsh and Ruddick (1995a) have shown that an R_ρ-dependent diffusivity introduces important modifications to the linearized intrusion model of Toole and Georgi (1981), so it seems plausible that nonconstant diffusivities may play an important role in modifying the behavior of large amplitude intrusions as well. In order that exponentially growing small amplitude solutions equilibrate at finite amplitude, fluxes of *T*, *S*, and momentum must adjust to slow growth rates when intrusions become large. This was a major motivation for allowing the diffusivities to vary continuously with R_ρ. However, we shall see that the key factor that makes equilibration possible is that the *T*–*S* ''flux ratio''—not the diffusivities per se—adjusts as the intrusions grow.

a. The model equations

Our purpose is to investigate the stability of a ''front'' characterized by large-scale horizontal and vertical *T*–*S* variations. The basic-state temperature, salinity, and alongfront velocity are described by the functions $\overline{T}_*(x_*, z_*)$, $\overline{S}_*(x_*, z_*)$, and $\overline{v}_*(x_*, z_*)$, which are assumed for simplicity to be linear functions (so the basic-state fields are uniform in the alongfront direction, with uniform gradients in the vertical and cross-front directions). The effects of rotation and alongfront shear are included for generality and to set the stage for future work, although we will not consider these effects in detail here. The equations governing the evolution of the velocity, temperature, and salinity fields are

$$\begin{aligned}
&\frac{\partial \mathbf{u}_*}{\partial t_*} + (\mathbf{u}_*\cdot\boldsymbol{\nabla}_*)\mathbf{u}_* + \mathbf{f}_*\times\mathbf{u}_* \\
&\quad = -\rho_{0*}^{-1}\boldsymbol{\nabla}_* p_* - \hat{z} g_* (\rho_* - \rho_{0*})/\rho_{0*} + (\boldsymbol{\nabla}_*\cdot A_*\boldsymbol{\nabla}_*)\mathbf{u}_* \\
&\frac{\partial S_*}{\partial t_*} + \mathbf{u}_*\cdot\boldsymbol{\nabla}_* S_* = \boldsymbol{\nabla}_*\cdot(K_{S*}\boldsymbol{\nabla}_* S_*) \\
&\frac{\partial T_*}{\partial t_*} + \mathbf{u}_*\cdot\boldsymbol{\nabla}_* T_* = \boldsymbol{\nabla}_*\cdot(K_{T*}\boldsymbol{\nabla}_* T_*) \\
&\boldsymbol{\nabla}_*\cdot\mathbf{u}_* = 0 \\
&\rho_* = \rho_{0*}[1 + \beta_*(S_* - S_{0*}) \\
&\qquad - \alpha_*(T_* - T_{0*})],
\end{aligned} \tag{2}$$

where starred ($_*$) quantities are dimensional, ρ_{0*} is the average density, f_* the Coriolis parameter, g_* the gravitational acceleration, $\mathbf{z}$ a unit vector in the vertical direction, α_* and β_* are thermal expansion and haline contraction coefficients, and A_*, K_{S*}, and K_{T*} are diffusivities for momentum, salt, and heat. Our aim is to examine the evolution of planar disturbances that can be considered one-dimensional in a suitably rotated frame of reference, like those discussed by Toole and Georgi (1981). Thus, we rewrite the set (2) in a coordinate frame in which the x_* (cross-front) axis is rotated through an angle θ, and the y (alongfront) axis through an angle ϕ (see Fig. 1). To represent the model in terms of a single spatial variable, we will require that the intrusion fields ($\tilde{u}$, $\tilde{v}$, $\tilde{S}$, and $\tilde{T}$) be laterally uniform in the rotated reference frame. The coordinate rotation is accomplished by projecting the above equations onto rotated coordinate vectors (see, for example, Morse and Feshback 1953). The rotated equations are

$$\frac{\partial u_*}{\partial t_*} - \underline{\overline{v}'_* \sin\phi \frac{\partial u_*}{\partial z_*}} - f_* \cos\phi \cos\theta v_* + g_* \sin\theta(\beta_* \tilde{S}_* - \alpha_* \tilde{T}_*) = \frac{\partial}{\partial z_*}\left(A_* \frac{\partial u_*}{\partial z_*}\right)$$

$$\frac{\partial v_*}{\partial t_*} - \underline{\overline{v}'_* \sin\phi \frac{\partial v_*}{\partial z_*}} + \cos\phi\left(u_* \frac{\partial \overline{v}_*}{\partial x_*} + v_* \frac{\partial \overline{v}_*}{\partial y_*}\right) + f_* \cos\phi \cos\theta u_* + g_* \sin\phi \cos\theta(\beta_* \tilde{S}_* - \alpha_* \tilde{T}_*) = \frac{\partial}{\partial z_*}\left(A_* \frac{\partial v_*}{\partial z_*}\right)$$

$$\frac{\partial S_*}{\partial t_*} - \underline{\overline{v}'_* \sin\phi \frac{\partial S_*}{\partial z_*}} + u_* \frac{\partial \overline{S}_*}{\partial x_*} + v_* \frac{\partial \overline{S}_*}{\partial y_*} = \frac{\partial}{\partial z_*}\left(K_{S*} \frac{\partial S_*}{\partial z'_*}\right)$$

$$\frac{\partial T_*}{\partial t_*} - \underline{\overline{v}'_* \sin\phi \frac{\partial T_*}{\partial z_*}} + u_* \frac{\partial \overline{T}_*}{\partial x_*} + v_* \frac{\partial \overline{T}_*}{\partial y_*} = \frac{\partial}{\partial z_*}\left(K_{T*} \frac{\partial T_*}{\partial z'_*}\right), \tag{3}$$

where (x_*, y_*, and z_*) are now the rotated coordinate axes, primed coordinates (x', y', z') represent the unrotated coordinate axes, and the model fields have been decomposed into a basic state (denoted by an overbar) plus an intrusive component (denoted by a tilde):

$$\begin{aligned} S_* &= \overline{S}_*(x_*, y_*, z_*) + \tilde{S}_*(z_*, t_*) \\ T_* &= \overline{T}_*(x_*, y_*, z_*) + \tilde{T}_*(z_*, t_*) \\ u_* &= \tilde{u}_*(z_*, t_*) \\ v_* &= \overline{v}_*(x_*, y_*, z_*) + \tilde{v}_*(z_*, t_*). \end{aligned} \tag{4}$$

Except for primed ($'$) velocities (which represent components along the original, unrotated axes), all velocities are now measured relative to the rotated coordinate axes. The y_*-dependence of the basic-state fields is a consequence of the alongfront rotation that was done since

$$\frac{\partial v_*}{\partial y_*} = \sin\phi\left(\cos\theta \frac{\partial v_*}{\partial z'_*} + \sin\theta \frac{\partial v_*}{\partial x'_*}\right). \tag{5}$$

Notice that the pressure does not appear in (3) because the intrusion pressure field is laterally uniform in the rotated reference frame—this also explains the absence of the lateral diffusive terms. The underscored terms in (3) represent advection by the basic-state flow across the rotated x_*, y_* coordinate planes (implying a mean vertical velocity in the rotated reference frame). Because $\overline{v}_*$ is a function of x_* and y_*, these terms introduce variations in u_*, v_*, S_*, and T_* with respect to x_* and y_* and will lead to alongfront tilting, in conflict with our assumption that intrusions are planar disturbances with a fixed orientation. Therefore, they are assumed for ''pragmatic'' reasons to be negligible and will be dropped. For our present purposes the underscored terms are irrelevant, since the basic-state flow vanishes by assumption. However, they may not be negligible in frontal environments with significant shear, and so the relevance of the model solutions should be carefully considered when the background flow $\overline{v}_*$ and the alongfront slope ($\tan\phi$) are nonzero. For Meddy Sharon, $\partial\overline{v}_*/\partial z_*$—a measure of the rate at which intrusive layers will be tilted in the alongfront direction—is of $O(10^{-3}\ \mathrm{s}^{-1})$, an order of magnitude greater than the growth rate of $\sim 10^{-4}\ \mathrm{s}^{-1}$ estimated by Walsh and Ruddick (1995a) [taken from their Eq. (38), assuming Pr = 1 and a constant K_S]. It is possible that only intrusions with no alongfront tilt ($\phi = 0$) can grow in such strongly sheared fronts. See May and Kelley (1997) for a detailed discussion of this topic.

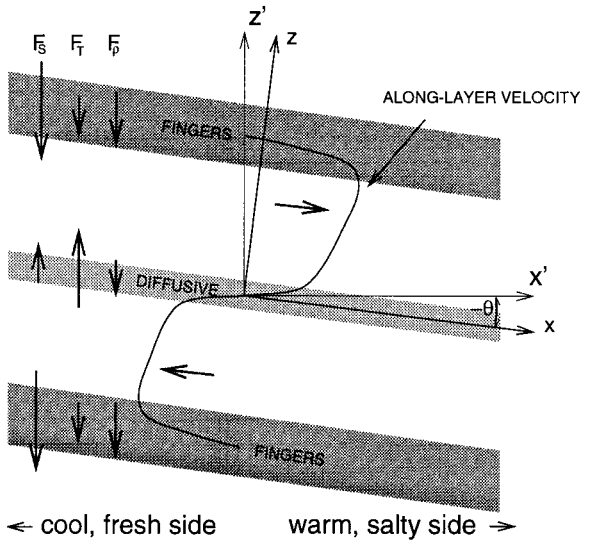

FIG. 1. Schematic of intrusion structure showing the alternating finger, diffusive, and unstably stratified layers that appear at large amplitude and the tilted coordinate system used by the numerical model. The x (cross-front) axis is rotated through an angle θ; the y axis (oriented into the page) is rotated through an angle ϕ. All perturbation fields are assumed independent of x and y in this rotated system.

After differentiating with respect to z and nondimensionalizing, the rotated equations become

$$u_{zt} - f\cos\phi\cos\theta v_z + \frac{\tan\theta}{\cos\phi}(1 + S_z - T_z) = [A(R_\rho)u_z]_{zz}$$

$$v_{zt} + u_z\overline{v}_x + v_z\overline{v}_y + f\cos\phi\cos\theta u_z + \tan\phi(1 + S_z - T_z) = [A(R_\rho)v_z]_{zz}$$

$$S_{zt} + u_z\overline{S}_x + v_z\overline{S}_y = [K_S(R_\rho)S_{z'}]_{zz}$$

$$T_{zt} + u_z\overline{T}_x + v_z\overline{T}_y = [K_T(R_\rho)T_{z'}]_{zz}$$

$$R_\rho \equiv \frac{T_{z'}}{S_{z'}}, \tag{6}$$

where S, T, and v are the total (basic state + disturbance) fields; z' is the true (unrotated) vertical axis; and the underscored terms in (3) have been dropped. The equations are written in terms of vertical gradients, as this allows gradient quantities such as R_ρ (and hence diffusivities) to be more easily computed. Notice that diffusive T–S fluxes are proportional to gradients along the unrotated (z') axis—this is because the small-scale processes fluxing T and S vertically are assumed to be sensitive to the ''true'' vertical gradients. In practice this will make little difference, however, because the angle between the z and z' axes is typically very small ($\approx 0.2°$ for our standard model run). The set (6) was made dimensionless using the basic-state buoyancy frequency, defined as

$$N_{0*} = \left(-\frac{g_*}{\rho_{0*}}\frac{\partial\overline{\rho}_*}{\partial z'_*}\right)^{1/2}, \tag{7}$$

and the maximum double-diffusive diffusivity, $K_{\max *}$. The following dimensionless quantities have been introduced:

$$t = N_{0*}t_*$$

$$z = z_*\sqrt{N_{0*}/K_{\max *}}$$

$$u_z = N_{0*}^{-1}\frac{\partial u_*}{\partial z_*}$$

$$v_z = N_{0*}^{-1}\frac{\partial v_*}{\partial z_*}$$

$$S_z = g_*\beta_* N_{0*}^{-2}\frac{\partial S_*}{\partial z_*}$$

$$T_z = g_*\alpha_* N_{0*}^{-2}\frac{\partial T_*}{\partial z_*}$$

$$K_S = K_{S*}/K_{\max *}$$

$$K_T = K_{T*}/K_{\max *}$$

$$A = A_*/K_{\max *}$$

$$\overline{S}_x = g_*\beta_* N_{0*}^{-2}\left[\cos\theta\frac{\partial\overline{S}_*}{\partial x'_*} + \sin\theta\frac{\partial\overline{S}_*}{\partial z'_*}\right]$$

$$\overline{S}_y = g_*\beta_* N_{0*}^{-2}\sin\phi\left[\cos\theta\frac{\partial\overline{S}_*}{\partial z'_*} - \sin\theta\frac{\partial\overline{S}_*}{\partial x'_*}\right]$$

$$\overline{T}_x = g_*\alpha_* N_{0*}^{-2}\left[\cos\theta\frac{\partial\overline{T}_*}{\partial x'_*} + \sin\theta\frac{\partial\overline{T}_*}{\partial z'_*}\right],$$

$$\overline{T}_y = g_*\alpha_* N_{0*}^{-2}\sin\phi\left[\cos\theta\frac{\partial\overline{T}_*}{\partial z'_*} - \sin\theta\frac{\partial\overline{T}_*}{\partial x'_*}\right]$$

$$\overline{v}_x = N_{0*}^{-1}\cos\phi\left[\cos\theta\frac{\partial\overline{v}'_*}{\partial x'_*} + \sin\theta\frac{\partial\overline{v}'_*}{\partial z'_*}\right]$$

$$\overline{v}_y = N_{0*}^{-1}\sin\phi\cos\phi\left[\cos\theta\frac{\partial\overline{v}'_*}{\partial z'_*} - \sin\theta\frac{\partial\overline{v}'_*}{\partial x'_*}\right]$$

$$f = \frac{f_{0*}}{N_{0*}}. \tag{8}$$

The quantities $\overline{S}_x$, $\overline{S}_y$, etc., represent basic-state gradients, as seen from the rotated coordinate frame, and primed coordinates (x', y', z') represent the unrotated coordinate axes.

In summary, the assumptions that allow us to get from (2) to (6) are (i) the intrusions are planar disturbances, (ii) the front is sufficiently wide that the intrusions do not ''feel'' its edges, and (iii) alongfront tilting of the intrusions by background shear is negligible. We will look for solutions to (6) that are periodic on the interval $(0, H)$, with H being the vertical scale of the model

domain. Notice that the only nonlinear terms in (6) are on the right-hand side and result from the amplitude dependence of the diffusivities and the viscosity (the functional forms of which will be specified shortly). The angles θ and ϕ must be specified prior to integrating these equations, and may be specified by appealing to linear instability calculations (e.g., Toole and Georgi 1981; McDougall 1985a,b; Walsh and Ruddick 1995a), or they may be chosen arbitrarily.

For the moment, we will not consider the influence of large-scale shear on the growing intrusions, so the alongfront momentum equation (6b) can be simplified by setting $\overline{v} = 0$. A consequence of this is that, by thermal wind, the basic-state density field must satisfy $\overline{\rho}_{x'} = 0$, and it follows that $\overline{T}_{x'} = \overline{S}_{x'}$ (note, however, that this is not true in the rotated frame, so $\overline{T}_x \neq \overline{S}_x$). Next, because McDougall (1985a,b) has shown that in this case the fastest-growing intrusions have no alongfront velocity component, (6b) can be further simplified by setting $v = 0$, since we intend to focus on the fastest-growing intrusions. This gives the simplified alongfront momentum balance

$$\tan\phi(1 + S_z - T_z) + f\cos\phi\cos\theta u_z = 0, \quad (9)$$

which is the thermal wind equation expressed in terms of the rotated axes, demonstrating that the cross-front velocity is in thermal wind balance when $v = 0$. Given that alongfront tilting of intrusive layers is likely to be important in fronts with strong vertical shear, a steady balance of this sort seems unlikely in many oceanic fronts—the actual alongfront momentum balance may involve Ekman dynamics. Regardless of the form of the alongfront momentum balance, the assumption $v = 0$ results in the simplified salinity, temperature, and cross-front momentum equations:

$$\begin{aligned} u_{zt} + \tan\theta(1 + S_z - T_z) &= [A(R_\rho)u_z]_{zz} \\ S_{zt} + u_z\overline{S}_x &= [K_S(R_\rho)S_{z'}]_{zz} \\ T_{zt} + u_z\overline{T}_x &= [K_T(R_\rho)T_{z'}]_{zz} \\ R_\rho &\equiv \frac{T_{z'}}{S_{z'}}, \end{aligned} \quad (10)$$

which form a closed set for u_z, S_z, and T_z [we have made the additional assumption that the alongfront slope is small, so $\cos\phi \approx 1$ in (6a)]. The model was coded for the set of equations (6), but since we have initialized with $v = 0$, the simplified set of equations (10) was in effect solved for all the runs shown here. The key assumption is that all disturbances are one-dimensional, with a cross-front slope θ that does not evolve with time.

For notational convenience, we will rewrite the parameters $\overline{S}_x$ and $\overline{T}_x$ in terms of the angle θ, the basic-state density ratio $\overline{R}_\rho$, and the dimensionless horizontal salinity gradient, $\overline{S}_{x'}$:

$$\begin{aligned} \overline{S}_x &= \left[\overline{S}_{x'}\cos\theta + \frac{\sin\theta}{\overline{R}_\rho - 1}\right] \\ \overline{T}_x &= \left[\overline{T}_{x'}\cos\theta + \frac{\overline{R}_\rho\sin\theta}{\overline{R}_\rho - 1}\right], \end{aligned} \quad (11)$$

where

$$\overline{R}_\rho \equiv \frac{\overline{T}_{z'}}{\overline{S}_{z'}}. \quad (12)$$

The fundamental parameters governing the model behavior will henceforth be taken to be $\overline{S}_{x'}$, $\overline{R}_\rho$, and the parameters related to mixing (which are discussed in the next section).

b. Specification of the viscosity and diffusivities

The fluxes of heat, salt, and momentum are parameterized using eddy coefficients, which are taken to be functions of the local *T*–*S* stratification. Because growing intrusions can eventually cause inversions in temperature and salinity, diffusivities must be specified for finger and diffusive-sense stratifications, as well as for non-double-diffusive conditions (see Fig. 2a). This sort of stratification-dependent parameterization is similar to that used by Zhurbas et al. (1987) in an investigation of the evolution of *T*–*S* disturbances under the action of double-diffusive and convective mixing. Our assumption is that in double-diffusively unstable conditions mixing is brought about by a linear combination of turbulence and double diffusion. We assume that there is a uniform level of ''background'' turbulence that is always active, with double diffusion adding to the turbulent fluxes when conditions are right. When the water column is stably stratified in both heat and salt, a small turbulent diffusivity (K_{turb}) is used, while a large diffusivity (K_{conv}) is used to ''convect'' away density inversions quickly. By ''small,'' we have in mind a (dimensional) diffusivity of the order of 1–2 ($\times 10^{-5}$ m^2 s^{-1}), similar to the value found by Ledwell et al. (1993), and Ledwell et al. (1994) in the North Atlantic Central Water, while ''large'' might correspond to the value of roughly 10^{-2} m^2 s^{-1} found by Chereskin (1995) for the mean viscosity in the mixed layer (although we will find that time step considerations prevent us from using such a large value in practice). In the appendix we examine the evolution of an overturn in a non-double-diffusive fluid and conclude that our crude parameterization of the mixing produced by density inversions does a good job of reproducing expected entrainment behavior.

We will consider two different cases for the diffusivity in double-diffusively unstable conditions, starting with the simplest case in which the diffusivities of heat and salt are constant within each stratification regime (i.e., finger, diffusive, stable, and convecting). Next we investigate the effect of allowing the diffusivities to vary

continuously with R_ρ in double-diffusively unstable conditions. In this case diffusivities are specified to be largest for R_ρ near unity and decrease monotonically away from $R_\rho = 1$. This behavior is in qualitative agreement with the inferences of Schmitt (1981) and Kelley (1984) from analyses of thermohaline staircase data. It is also reminiscent of the turbulence-modified salt finger flux laws proposed by Kunze (1994), who suggested that faster-growing fingers near $R_\rho = 1$ are able to grow larger before being disrupted by intermittent turbulence, so their fluxes (and the corresponding diffusivities) should be larger as well. While the above studies lend qualitative support to our flux formulations, the formulations are fundamentally ad hoc, since they have not been well constrained by observations. The fluxes of T and S due to double diffusion are linked via the flux ratios γ_d and γ_f (assumed constant), defined as

$$\gamma_f = \left(\frac{\alpha_* F_{T*}^{\text{fingers}}}{\beta_* F_{S*}^{\text{fingers}}}\right)$$

$$\gamma_d = \left(\frac{\beta_* F_{S*}^{\text{diffusive}}}{\alpha_* F_{T*}^{\text{diffusive}}}\right), \tag{13}$$

where F_{T*} and F_{S*} are double-diffusive fluxes of T and S. Both flux ratios must be less than one so that double-diffusive convection can lower the potential energy of the water column, and it follows that double-diffusive density fluxes are upgradient.

Following Ruddick (1985), momentum fluxes produced by double-diffusive convection are assumed to be proportional to buoyancy fluxes, allowing the eddy viscosity [$A(R_\rho)$] to be expressed in terms of the density diffusivity and a Prandtl number (Pr). However, Ruddick's arguments have not been confirmed, and the rate at which momentum is transferred by double-diffusive convection is still uncertain, so we will also discuss a run in which double-diffusive momentum fluxes are proportional to salt fluxes (for salt fingers) and to heat fluxes (for diffusive convection). As for the case of T and S, a constant eddy viscosity (equal for heat and salt) is used when conditions are double-diffusively stable. The same Prandtl number is used for double-diffusive and non-double-diffusive conditions. While this is probably not strictly correct, uncertainties surrounding momentum flux parameterizations make using a more complex parameterization seem questionable.

The model diffusivities are given by

(A) *Salt fingers* ($\partial\rho/\partial z' < 0$, $1 < R_\rho < \infty$):

$$K_S^F(R_\rho) = R_\rho^{-n_f} \quad \text{(salt diffusivity due to fingers)} \tag{14}$$

$$K_S(R_\rho) = K_S^F(R_\rho) + K_{\text{turb}} \quad \text{(total salt diffusivity)}$$

$$K_T(R_\rho) = \gamma_f K_S^F(R_\rho)/R_\rho + K_{\text{turb}} \quad \text{(``temperature'' diffusivity)}$$

$$A(R_\rho) = \begin{cases} \Pr\left(\dfrac{1-\gamma_f}{R_\rho - 1} K_S^F(R_\rho) + K_{\text{turb}}\right) & \text{(i) Ruddick (1985) viscosity formulation} \\ \Pr[K_S^F(R_\rho) + K_{\text{turb}}] & \text{(ii) momentum flux } \sim \text{ salt flux} \end{cases}$$

(B) *Diffusive stratification* ($\partial\rho/\partial z' < 0$, $0 < R_\rho < 1$):

$$K_T^D(R_\rho) = R_\rho^{n_d}$$

$$K_T(R_\rho) = K_T^D(R_\rho) + K_{\text{turb}}$$

$$K_S(R_\rho) = \gamma_d R_\rho K_T^D(R_\rho) + K_{\text{turb}}$$

$$A(R_\rho) = \begin{cases} \Pr\left(\dfrac{1-\gamma_d}{1-R_\rho} R_\rho K_T^D(R_\rho) + K_{\text{turb}}\right) & \text{(i) Ruddick (1985) viscosity formulation} \\ \Pr[K_T^D(R_\rho) + K_{\text{turb}}] & \text{(ii) momentum flux } \sim \text{ salt flux} \end{cases}$$

(C) *Stable in T and S* ($\partial\rho/\partial z' < 0$, $R_\rho < 0$):

$$K_S = K_T = K_{\text{turb}}$$

$$A = \Pr \cdot K_{\text{turb}}$$

(D) *Statically unstable* ($\partial\rho/\partial z' \geq 0$):

$$K_S = K_T = K_{\text{conv}}$$

$$A = \Pr \cdot K_{\text{conv}},$$

where K_{turb} is the diffusivity associated with ''background'' turbulence, and K_{conv} is the large diffusivity

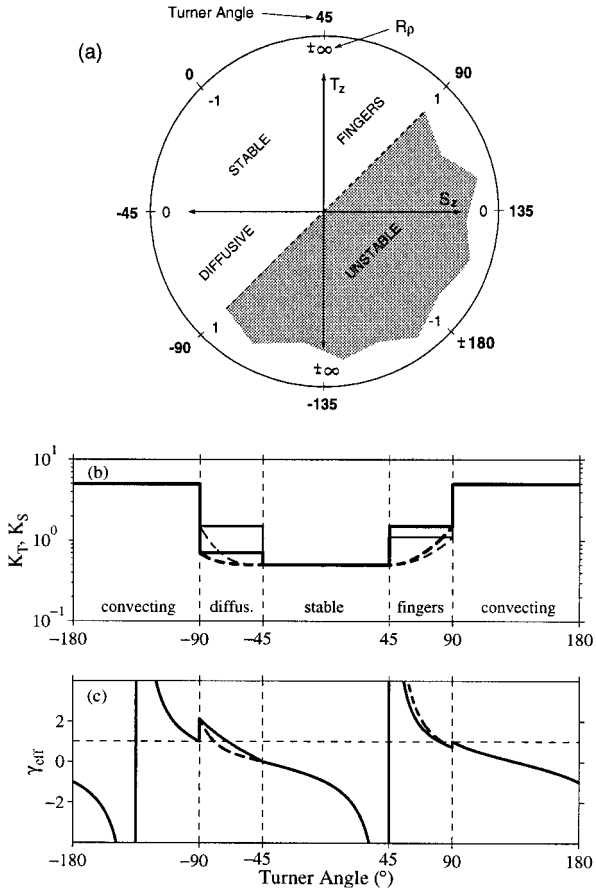

FIG. 2. (a) Plot showing diffusivity parameterizations in different regions of (S_z, T_z) space. (b) The diffusivities K_T (thin line) and K_S (thick) as functions of the Turner angle. In statically unstable regions a large (constant) eddy diffusivity is chosen; in finger and diffusive stratifications the diffusivities of heat and salt are unequal. Solid curves show the constant double-diffusive diffusivity case; dashed lines show the case in which double-diffusive diffusivities are continuous functions of R_ρ ($n_f = 2$, $n_d = 3$—see text for details). (c) The turbulence-modified *T–S* flux ratio for the same parameter values (the horizontal dashed line is at $\gamma_{eff} = 1$).

used to mix away density inversions in statically unstable (''convecting'') regions. The Prandtl number Pr is equal to A/K_ρ for Ruddick's (1985) formulation, or A/K_S for the alternate viscosity formulation in (14). The salt finger flux ratio γ_f ($\approx$0.6: Schmitt 1979) and the diffusive flux ratio γ_d ($\approx$0.2: Turner 1965) are assumed to be constant. More general R_ρ-dependent formulations are possible (see, e.g., Turner 1965; Stern 1975; Kelley 1984), but we will show that the background turbulence causes the effective (turbulence-modified) *T–S* flux ratio to increase with R_ρ even when γ_f and γ_d are constant. Using the above diffusivity formulations, the set (10) allows intrusion growth if the water column is finger stratified (warm and salty over cool and fresh) or diffusively stratified (cool and fresh over warm and salty) but not if the stratification is stable in both properties [since in this case the diffusivities of heat and salt are equal, according to (14c)].

The exponents n_f and n_d determine how rapidly the diffusivities decrease away from $R_\rho = 1$. The default values for n_f and n_d are taken to be zero (i.e., constant K_S and K_T for each different type of stratification), but we will also consider the case in which they are set equal to 2 and 3, respectively. We do not claim that these values are correct—our intent is only to investigate the qualitative effect of R_ρ-dependent diffusivities. However, the exponents we use do give diffusivities qualitatively like those reported by Schmitt (1981) and Kelley (1984) for thermohaline staircases. The diffusivities K_T and K_S given by (14) are plotted in Fig. 2b as functions of R_ρ and the Turner angle [for the cases $n_f = n_d = 0$ (solid curve) and $n_f = 2$, $n_d = 3$ (dashed)], defined as

$$Tu = \tan^{-1}\left(\frac{S_z + T_z}{S_z - T_z}\right) \tag{15}$$

(Ruddick 1983) for the parameter values $K_{turb} = 0.3$ and $K_{conv} = 5$. The total (turbulence-modified) *T–S* flux ratio [given by (22)] for the same parameter values is shown in Fig. 2c. Notice that when n_f and n_d are nonzero (dashed curves in Fig. 2b), diffusivities decrease away from $R_\rho = 1$ for both diffusive and finger-sense stratifications. Choosing this form for the diffusivity should lead to an enhanced *T–S* flux divergence for growing intrusions similar to that discussed by Schmitt (1981) and Walsh and Ruddick (1995a,b), which should cause the fastest-growing intrusions to have larger growth rates and vertical scales than in the constant diffusivity case.

The flux formulations in (14) are based on the assumption that turbulence does not disrupt double-diffusion significantly, which is in contradiction with laboratory experiments by Linden (1971) and with the model proposed by Kunze (1994) for salt finger fluxes in the presence of turbulence. However, the linear superposition of double-diffusive and turbulent fluxes is probably justified if the turbulence is highly intermittent, so that there are long periods with no turbulence during which salt fingers can grow unobstructed. In addition, our assumption that turbulent and double-diffusive fluxes are additive appears to be consistent with experiments done by Crapper (1976), who hypothesized that fluxes across a diffusive interface could be represented by a linear combination of turbulent entrainment and diffusive convection and found that the predicted *T–S* flux ratios that follow from this assumption were in good agreement with experimental data. Crapper found that the effective *T–S* flux ratio increased from being less than one for small values of the interfacial density ratio to larger than one for large density ratio values, similar to the behavior in Fig. 2c.

Table 1 summarizes typical values for the model parameters, chosen to be roughly appropriate for Meddy

TABLE 1. Estimated values for the parameters that appear in the model equations, chosen to be appropriate for Meddy Sharon.

K_{S*}	3×10^{-5} m^2 s^{-1}	Salt diffusivity
$K_{\text{turb}*}$	$1 - 2 \times 10^{-5}$ m^2 s^{-1}	''Background'' turbulent diffusivity
$\partial\bar{S}_*/\partial x'_*$	5×10^{-5} psu m^{-1}	Horizontal salinity gradient
$\bar{S}_{x'}$	0.06	Dimensionless horizontal salinity gradient
$\bar{R}_\rho$	1.6	Density ratio (lower half of Meddy)
$\bar{R}_\rho$	0.8	Density ratio (upper half)
N_{0*}	2.5×10^{-3} s^{-1}	Buoyancy frequency
γ_f	0.6	Salt finger flux ratio
γ_d	0.2	Diffusive flux ratio
α_*	1.8×10^{-4} °C^{-1}	Thermal expansion coefficient
β_*	7.5×10^{-4} psu^{-1}	Haline contraction coefficient

Sharon (e.g., see Hebert 1988; Ruddick and Hebert 1992). The value of $K_{\text{turb}*}$ is a typical diffusivity for the deep ocean (Ledwell et al. 1993, 1994), and γ_d and γ_f are derived from laboratory experiments (Turner 1965; Schmitt 1979). Certain quantities that are difficult or impossible to deduce from observations (e.g., n_f, n_d, and Pr) are not listed in Table 1; our approach has been to try several different values for these parameters. The value of the maximum double-diffusive diffusivity ($K_{\max*}$) was inferred in such a way as to give an average value for K_{S*} equal to that listed in Table 1.

c. Discretization

The model equations were discretized using a Crank–Nicholson (semi-implicit) scheme for the diffusion terms. Crank–Nicholson is unconditionally stable for diffusion problems, although it requires that a matrix inversion be performed at each time step. Nevertheless, the model executes quickly because the domain is one-dimensional, and there are only 200 grid points for most model runs. Discretization of the system (10) under the Crank–Nicholson scheme combined with periodic boundary conditions results in a tridiagonal matrix with nonzero elements in the upper-right and lower-left corners. This was written as the sum of a tridiagonal matrix plus the outer product of two sparse vectors, and the Sherman–Morrison formula (Press et al. 1986, section 2.10) was used to invert the system efficiently. Because the diffusivities and the viscosity evolve with time, they must be recalculated at each time step. Rather than treating the diffusivities as explicit terms (i.e., using the current diffusivities to compute the S, T, and velocity fields at the next time step), we perform an initial time step to see how the diffusivities evolve, then use the average diffusivity at each grid point to time step the fields.

There are a number of factors to consider in selecting an appropriate time step for the model runs. First, it is necessary to accurately reproduce the growth rates predicted by linear theory. The model runs suggest that growth rates can be reproduced to about 10% accuracy using only 10 time steps per linear growth period. We typically perform several hundred time steps per growth period, so this is not a serious constraint. However, to ensure reasonable accuracy throughout the calculation we require that neither salt, heat, nor momentum diffuse ''too far'' (farther than the grid spacing) during a single time step. Thus, we choose the model time step to be less than the diffusive timescale based on the maximum diffusivity, which gives the constraint

$$\Delta t < \frac{(\Delta z)^2}{K_{\text{conv}}}. \tag{16}$$

We see that the value of K_{conv} is important in determining the maximum allowable Δt. Physically, we would like to choose K_{conv} as large as possible so that density inversions are mixed away rapidly. However, the above constraint on Δt leads us to choose an intermediate value of 5 for a 200-point model grid. Runs not satisfying the inequality (16) typically exhibit some form of numerical instability, although usually not until after convecting layers appear. As a measure of the numerical accuracy of the runs, we use the conservation statements

$$\frac{\partial}{\partial t}\langle u_z\rangle = \frac{\partial}{\partial t}\langle S_z\rangle = \frac{\partial}{\partial t}\langle T_z\rangle = 0, \tag{17}$$

where the notation $\langle\cdot\rangle$ denotes a vertical average over the model domain. These expressions follow directly from (10) and the requirement that the solutions be periodic in the vertical. In the model runs shown, $\langle S_z\rangle$ and $\langle T_z\rangle$ were conserved to within 0.5% over the course of a run.

d. Model initialization and validation: Linear theory

Because the intrusion slope and the vertical scale of the domain must be specified, a systematic way of choosing these parameters is needed. The slope and wavelength can be chosen at random, but the resulting model solution might then bear little resemblance to what would be seen in the ocean. Therefore, we will assume that the disturbances that grow most rapidly at small amplitude also dominate at large amplitude and hence determine the structure of oceanic interleaving. With this assumption, the model runs can be initialized with plausible values of slope and wavelength for any combination of model parameters. In this section, we solve the linear instability problem for the set (10) and

use the results of the analysis to validate the model output and, in later sections, as a tool for initializing the model runs.

To test the numerical model, growth rates predicted by linear theory are compared with measured growth rates of small-amplitude model solutions. We make use of the growth rate polynomial for the set (10) (assuming a finger-favorable basic-state stratification), obtained by substituting solutions of the form

$$\mathbf{V}e^{i(kx+mz)+\lambda t} \tag{18}$$

into the linearized form of (10) [and making use of (14a)]. Equation (10) is thus reduced to a matrix equation for the amplitudes $\hat{u}$, $\hat{S}$, and $\hat{T}$:

$$\mathbf{A}\cdot\mathbf{V} = \lambda\mathbf{I}\cdot\mathbf{V}$$

$$\mathbf{V} = \begin{pmatrix}\hat{u}\\ \hat{S}\\ \hat{T}\end{pmatrix}. \tag{19}$$

The eigenvalues of $\mathbf{A}$ represent intrusion growth rates, and the relative sizes of $\hat{u}$, $\hat{S}$, and $\hat{T}$ are determined by the corresponding eigenvectors. The growth rate polynomial is

$$\begin{aligned}&\lambda^3 + \lambda^2 M^2[1 + \mathrm{Pr} + (\gamma_{\mathrm{eff}} - \overline{R}_\rho)K_S'/K_S + \gamma_{\mathrm{eff}}']\\ &\quad + \lambda\{\mathrm{Pr}M^4[1 + (\gamma_{\mathrm{eff}} - \overline{R}_\rho)K_S'/K_S + \gamma_{\mathrm{eff}}'] + s^2\}\\ &\quad + \gamma_{\mathrm{eff}}'\mathrm{Pr}M^6 - [1 + (1 - \overline{R}_\rho)K_S'/K_S]\\ &\quad \times M^2 s[\varepsilon_x - s(1 + \varepsilon_z)] - \gamma_{\mathrm{eff}}' s M^2(\varepsilon_x - s\varepsilon_z)/\varepsilon_z = 0,\end{aligned} \tag{20}$$

where primes denote differentiation with respect to R_ρ, and the following dimensionless quantities have been introduced:

$$\begin{aligned}\lambda &= \lambda_*/N_{0*}\\ M &= m_*\sqrt{K_{S*}/N_{0*}} = m\sqrt{K_{S*}/K_{\max *}}\\ s &= k_*/m_* = -\tan\theta\\ \mathrm{Pr} &= A_*(\overline{R}_\rho)/K_{S*}(\overline{R}_\rho) \rightarrow \text{Prandtl number}\\ \varepsilon_x &= (1 - \gamma_{\mathrm{eff}}) \times \overline{S}_{x'}\\ \varepsilon_z &= (1 - \gamma_{\mathrm{eff}}) \times \overline{S}_{z'}.\end{aligned} \tag{21}$$

All quantities in (20) are evaluated at $R_\rho = \overline{R}_\rho$. The notation γ_{eff} denotes the turbulence-modified ''effective'' *T–S* flux ratio. Because turbulence is characterized by a flux ratio that increases with R_ρ ($\alpha_* F_{T*}^{\mathrm{turb}}/\beta_* F_{S*}^{\mathrm{turb}} = R_\rho$), the flux ratio of a linear superposition of turbulence and double diffusion is also an increasing function of R_ρ:

$$\left(\frac{\alpha_* F_{T*}}{\beta_* F_{S*}}\right) \equiv \gamma_{\mathrm{eff}}(R_\rho) = \frac{\gamma_{\mathrm{f}} K_S^F(R_\rho) + R_\rho K_{\mathrm{turb}}}{K_S^F(R_\rho) + K_{\mathrm{turb}}}. \tag{22}$$

Notice that γ_{eff} reduces to the salt finger flux ratio γ_{f} when $K_{\mathrm{turb}} = 0$.

The growth rate expression (20) generalizes Eq. (13) from Walsh and Ruddick (1995a) to include a nonconstant flux ratio. This expression is similar to that derived by Hebert (1998, submitted to *J. Phys. Oceanogr.*) for the case of differential mixing of heat and salt due to ''incomplete'' turbulent mixing, as well as to the polynomial derived by Holyer (1983) using molecular diffusivities for *T* and *S*. The expression (20) is somewhat more general, though, as it is not limited to the constant diffusivity case, nor to a specific form for γ_{eff}. The differential mixing case can be obtained from (20) by setting $K_S' = 0$ and $\gamma_{\mathrm{eff}} = R_\rho K_T/K_S$.

The growth rate polynomial (20) provides a systematic way of initializing the model with the fastest-growing disturbance for cases in which the stratification is finger favorable. When the water column is diffusively stratified, a *T–S* symmetry in (10) exists [as discussed by Walsh and Ruddick (1995a)], which allows the linear results for the finger case to be transformed to give the corresponding slope, wavenumber, and growth rate for a diffusive-sense basic-state stratification. Although their analysis did not consider the case in which turbulence and double diffusion are both present, the transformation is also valid in this case.

In Fig. 3a the growth rates are contoured for the case $\overline{R}_\rho = 1.6$, Pr = 10, $\epsilon_x = 0.032$ (or equivalently $\overline{S}_{x'} = 0.08$), $n_{\mathrm{f}} = 2$, and $K_{\mathrm{turb}} = 0.3$, as functions of the slope *s* and the vertical wavenumber *m*. For each value of *s* and *m*, the root of (20) with the largest real part is shown. In Fig. 3c the rms salinity amplitude of the fastest-growing intrusion is plotted as a function of time. The initial amplitude of the salinity perturbation ($\hat{S}$) was $\hat{S}m/\overline{S}_z \approx 0.002$. Until $t = 4000$ the growth appears to be purely exponential, and the best-fit slope between $t = 300$ and $t = 3300$ (0.00164, corresponding to an *e*-folding period of about 600) agrees with the growth rate predicted by linear theory to three significant digits. In Table 2 we compare the model growth rate with linear theory for the labeled points in Fig. 3. The agreement is excellent, indicating that the model accurately reproduces the behavior of the linear system for small-amplitude disturbances. The dimensional wavelength of the fastest-growing intrusion is

$$\frac{2\pi}{m}\sqrt{\frac{K_{S*}}{N_{0*}}} \approx 18 \text{ m},$$

in reasonably good agreement with Ruddick and Hebert's (1988) measured wavelength of 25 m for the lower-half of Meddy Sharon. The *e*-folding timescale for growth is $(\lambda N_{0*})^{-1} \approx 2.8$ days.

The extremely close agreement with linear theory until $t \approx 4000$ is somewhat surprising, since inversions occurred in the salinity field at $t \approx 3600$ and convecting layers appeared at $t \approx 4600$. Before inversions appear the dominant nonlinear effect has been to ''skew'' the

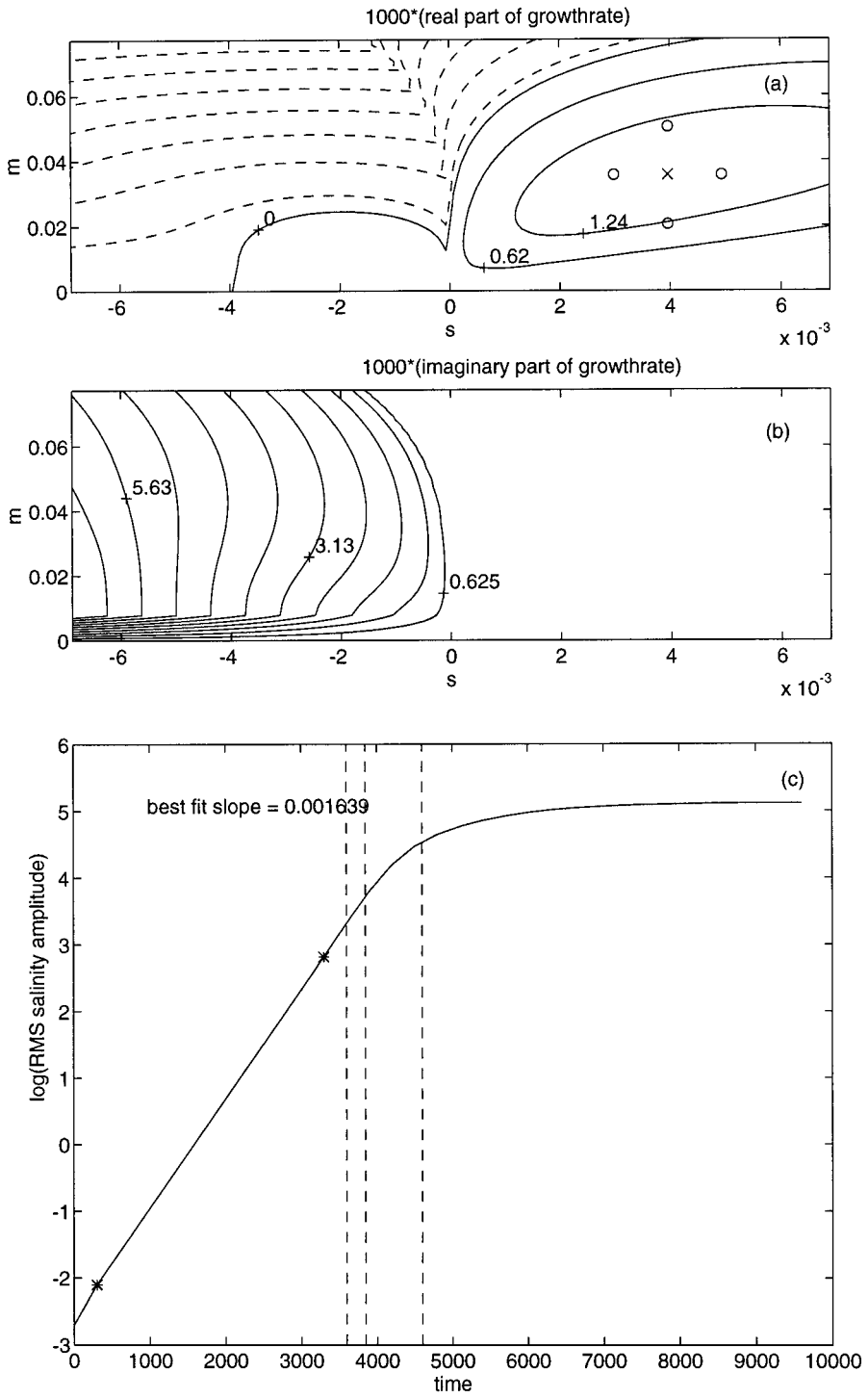

FIG. 3. Contour plot of the real (a) and imaginary (b) parts of the growth rate predicted by linear theory as a function of the slope s and the vertical wavenumber m for the parameter values $\overline{R}_\rho = 1.6$, $Pr = 10$, $\overline{S}_{x'} = 0.08$, $n_f = 2$, and $K_{\text{turb}} = 0.3$. Dashed contours indicate negative growth rates; growth rates with nonzero imaginary part are associated with oscillatory solutions. The "×" in (a) shows the location of the most unstable disturbance; the "×" and the small circles mark the locations of the runs summarized in Table 1. (c) The evolution of the salinity disturbance amplitude, with vertical lines marking the appearance of nondouble diffusive ($t \approx 3600$), diffusively stratified ($t \approx 3800$), and convecting regions ($t \approx 4600$). The slope of the curve in panel c gives the growth rate, which is in excellent agreement with linear theory until $t \approx 4000$.

TABLE 2. Measured growth rates for small-amplitude disturbances from several model runs, along with the growth rates predicted by linear theory. The runs correspond to the labeled points in Fig. 3. The model growth rates are in excellent agreement with linear theory.

θ°	m	Observed λ	Predicted λ
−0.2269	0.0356	0.001639	0.001642
−0.2826	0.0356	0.001600	0.001602
−0.1712	0.0356	0.001582	0.001582
−0.2269	0.0504	0.001337	0.001340
−0.2269	0.0206	0.001208	0.001207

velocity profile, increasing the shear in the diffusive region and decreasing that in the finger region. This demonstrates that even when the intrusion amplitude is quite large, the growth rate does not change appreciably until density overturns occur. Thus, linear theory seems to hold well beyond the point where it can be considered formally valid. Walsh and Ruddick (1995a) showed that a nonconstant viscosity $A(R_\rho)$ does not affect linear growth rates. However, one might expect that after intrusions grow beyond the point where linear theory is formally valid, R_ρ variations could modify $A(R_\rho)$ significantly, changing the momentum flux convergences predicted by linear theory and hence altering the growth rate. The reason why this does not happen appears to be that the modified momentum fluxes at the nonlinear stage produce almost no *net* momentum flux out of an intrusion, they only redistribute momentum in the vertical, hence skewing the velocity profile without affecting the overall growth rate.

To verify that focusing on the fastest-growing small amplitude disturbance is reasonable, a run was done in which $\tilde{u}_z$, $\tilde{v}_z$, $\tilde{S}_z$, and $\tilde{T}_z$ were initialized with infinitesimal, random disturbances. This allows an investigation of interactions between intrusions with various wavelengths as they grow to large amplitude. The randomly generated fields had white wavenumber spectra, and the slopes of all spectral components were set equal to that of the fastest-growing mode (FGM). Two different initializations were used: first, the domain was chosen to be an integral number times the wavelength of the FGM, then a run was done for which the vertical domain and the wavelength of the FGM were incommensurate. In the first case, the FGM soon dominated over the entire domain, and solutions looked like those initialized with the FGM. For the case in which the vertical domain and the FGM are incommensurate (the domain was chosen to be ~3.35 times the wavelength of the FGM) the FGM ''tries'' to grow, but the periodicity requirement forces the wavelength to vary over the model domain, so the growth rate is reduced by roughly 5%. Hence, we conclude that if the vertical scale of the model domain is commensurate with the wavelength of the FGM, then initializing model runs with the FGM is not significantly different than initializing with broadband noise. However, the results are somewhat more sensitive to the height chosen for the model domain.

3. Intrusion evolution

In this section we investigate the character of the model solutions. Our approach is to show a ''standard'' run, using what we believe are plausible parameter values, and examine the mechanics behind the evolution of the model fields and their approach to equilibrium. We then look at the influence of nonconstant finger- and diffusive-sense diffusivities on the steady solutions, using a run in which the R_ρ dependence is ''turned on'' [i.e., the exponents n_f and n_d in (14) are nonzero]. All the runs in this section use Ruddick's (1985) viscosity formulation; in section 4d we will discuss the effect of using the alternative viscosity formulation discussed in section 2b.

The mesh plots in Fig. 4 show the evolution of the model fields for a run with parameter values $\overline{R}_\rho = 1.6$, $K_{\text{turb}} = 0.5$, $K_{\text{conv}} = 5$, Pr = 10, $\overline{S}_{x'} = 0.05$, $n_f = n_d = 0$, $\gamma_f = 0.6$, and $\gamma_d = 0.2$; 200 grid points were used in the vertical. A value of 0.5 for K_{turb} corresponds to the case in which turbulent salt fluxes are half as large as double-diffusive fluxes, roughly in agreement with the values quoted in Table 1. The perturbation used to initialize the run corresponds to the fastest growing instability predicted by linear theory. Figure 4a shows the cross-front velocity u; Figs. 4b and 4c show the evolution of the salinity and density fields, respectively. Initially the growth of all three fields is exponential, but growth slows dramatically when convecting layers (shown by the plateaulike regions in Fig. 4c) form. This effect is most evident in the velocity field (Fig. 4a), where growth essentially halts when convecting layers appear, indicating that convection exerts a strong ''drag'' on the intrusions.

Figure 5 shows the time evolution of the layer thicknesses for the run shown in Fig. 4. Initially the fluid is finger stratified at all depths. At $t = 5900$ a stable (i.e., non-double-diffusive) layer appears, which grows until $t \approx 6400$, when a diffusively stratified layer forms. This erodes fluid away from the stably stratified region until $t \approx 7100$, when the stable layer disappears and is replaced by a statically unstable layer, which thickens rapidly by ''entraining'' fluid from the finger region. Notice that the thickness of the diffusive layer is very nearly constant after a brief initial growth period. After a temperature inversion appears within the stably stratified region, the resulting diffusive layer thickens rapidly until it occupies the entire region of the water column that had been stably stratified. At this point, convection begins and the diffusive layer stops growing, and its thickness remains essentially constant thereafter. The convecting layers continue entraining from finger-stratified regions until $t \approx 12\,000$, when entrainment stops.

Figure 6a shows the evolution of the run shown in Fig. 4 in the T–S plane. Initially the T–S curve is straight (since $\overline{R}_\rho$ is constant), but the growing intrusions soon produce small wiggles. At $t = 6600$, after diffusive layers form, the T–S curve has the ''sawtooth'' character

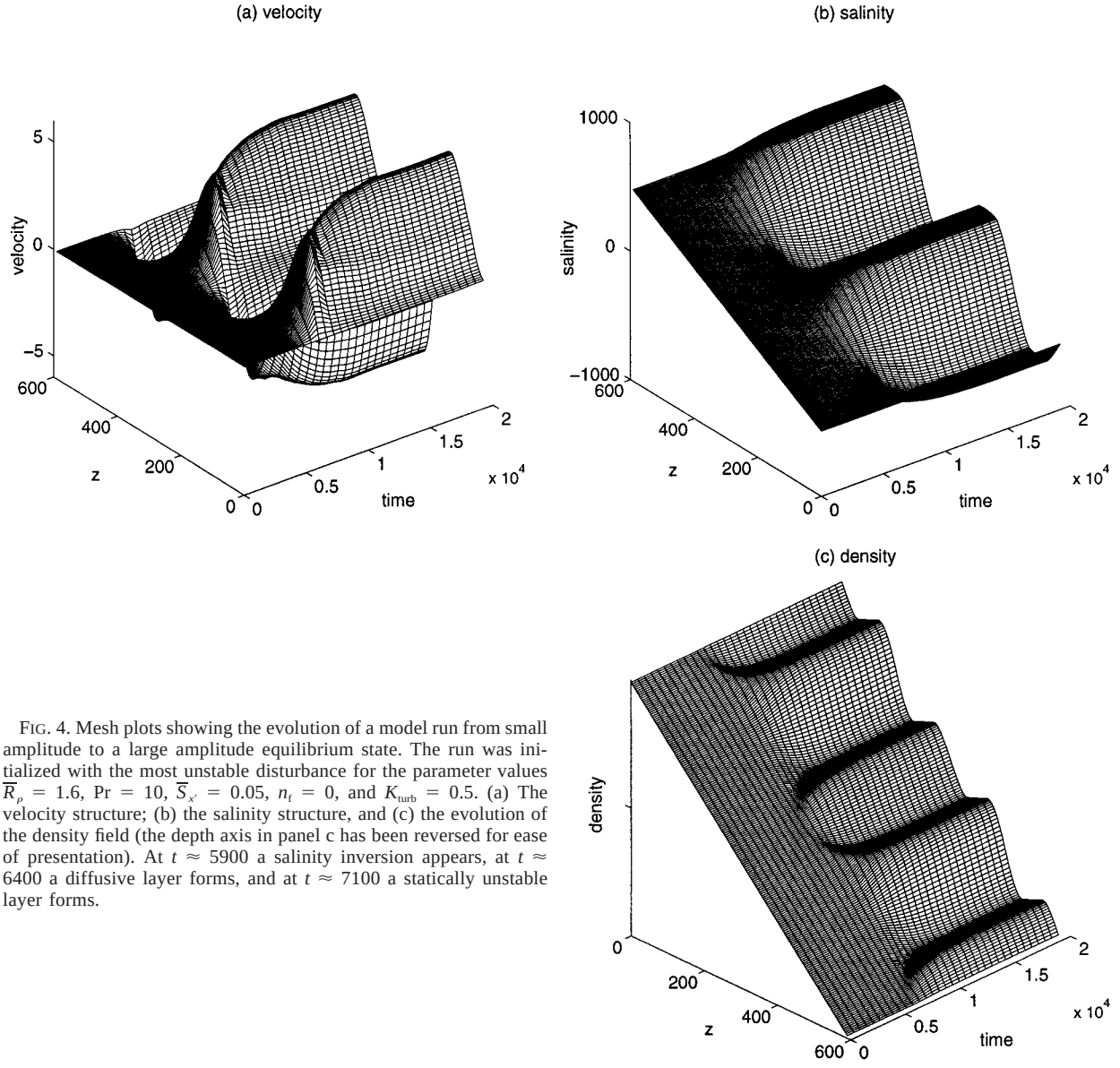

FIG. 4. Mesh plots showing the evolution of a model run from small amplitude to a large amplitude equilibrium state. The run was initialized with the most unstable disturbance for the parameter values $\overline{R}_\rho = 1.6$, Pr = 10, $\overline{S}_{z'} = 0.05$, $n_f = 0$, and $K_{\text{turb}} = 0.5$. (a) The velocity structure; (b) the salinity structure, and (c) the evolution of the density field (the depth axis in panel c has been reversed for ease of presentation). At $t \approx 5900$ a salinity inversion appears, at $t \approx 6400$ a diffusive layer forms, and at $t \approx 7100$ a statically unstable layer forms.

typically taken to be the signature of thermohaline intrusions. The ''loops'' in the *T–S* curve at $t = 18\,600$ are the signatures of convecting layers. These loops are reminiscent of those reported by Posmentier and Houghton (1978), who found evidence of localized overturns associated with double-diffusive convection (however, their precise observation is difficult to verify because of sensor time-response effects). Washburn and Gibson (1984) have also observed *T–S* loops like those in Fig. 6a in horizontal sections taken at the base of the mixed layer, which they attribute to horizontal stirring processes. In the latter stages of the run shown in Fig. 6a (when the *T–S* curve has a sawtooth appearance), both the diffusive and finger regions tend toward $R_\rho = 1$, as a result of the quasi-isopycnal advection across the front. The *T–S* curve appears straight within the finger and diffusive layers, suggesting a nearly constant R_ρ within each of these regions. However, significant R_ρ variations occur in the vicinity of the loops, and we will show in section 4b that depth variations in R_ρ within the finger and diffusive layers are essential to equilibration, as they allow a depth-varying *T–S* flux ratio.

Some additional insight can be gained by observing the model evolution in the (S_z, T_z) plane (Fig. 6b). The dotted lines through the origin have constant R_ρ, and the shaded region has $N^2 < 0$ (the legend is identical to that for panel a). The initial condition (shown by the shaded dot) has nearly constant gradients. Initially the fields evolve in a nearly isopycnal fashion (lines of constant N^2 have slope = 1) within the salt finger sector,

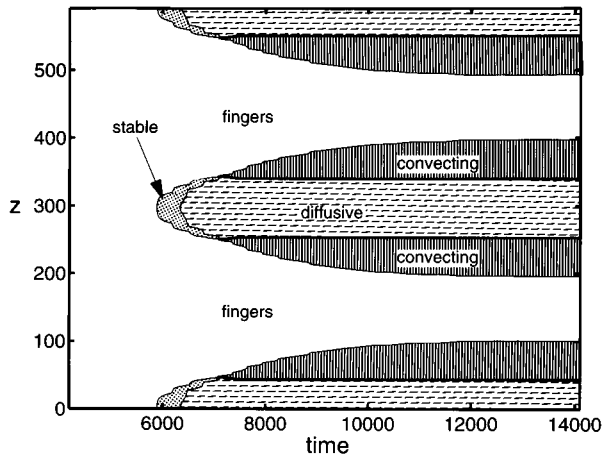

FIG. 5. Evolution of layer thicknesses for the model run shown in Fig. 4. At $t \approx 5900$ a stably stratified layer appears, which grows in thickness until $t \approx 6400$, when a diffusive layer forms. The diffusive region grows thicker by ''entraining'' fluid from the stably stratified layer. At $t \approx 7100$ the stable layer disappears entirely and is replaced by a statically unstable layer that thickens with time, primarily at the expense of the finger layer.

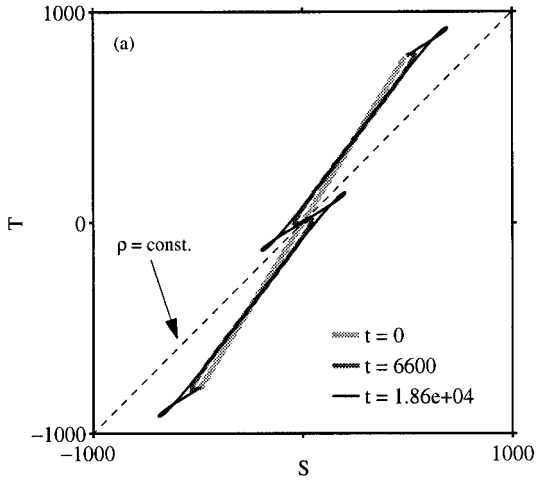

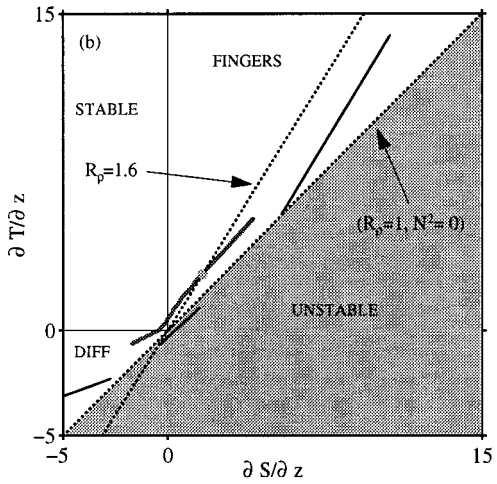

FIG. 6. (a) Evolution of the standard model run in *T–S* space. Initially the *T–S* curve is straight, but the growing intrusions soon cause ''wiggles'' to appear. By $t = 6600$ the intrusions have become large enough that inversions in *T* and *S* appear. The ''loops'' evident at $t = 18\,600$ result from unstably stratified ''convecting'' layers. (b) The same three profiles shown in (a) are plotted in the (S_z, T_z) plane. At $t = 0$ (shown by the shaded dot) gradients are nearly constant, and the initial evolution is nearly isopycnal, with stable and diffusively stratified layers appearing by $t = 6600$ (shaded line). At equilibrium ($t = 18\,600$: dark line), the gradients of *T* and *S* are discontinuous.

so increased salinity gradients are associated with smaller values of R_ρ, and decreased gradients with larger R_ρ values (this will also be evident in Fig. 7, where vertical profiles from the run are shown). After convecting layers form, *T–S* gradients become discontinuous, as shown by the thin black line segments corresponding to equilibrium state. These discontinuities result from the ''jumps'' in diffusivity between stratification regimes inherent in our diffusivity formulation (14)—a jump in diffusivity requires a corresponding gradient jump for flux continuity. It is of interest to note that the discontinuities apparent in panel b are not evident in the corresponding *T–S* profiles in panel a (which appears to be both continuous and smooth)—the *T–S* representation obscures this feature of the profiles. At equilibrium there is a marked variation in R_ρ within all three layers, and within the finger and diffusive layers $R_\rho \approx 1$ adjacent to the convecting layers and reaches a maximum at the center of the layers. The fact that the segments making up the equilibrium (S_z, T_z) profile appear to be linear is a direct consequence of the form of the flux laws, as will be discussed in section 4b.

Detailed vertical profiles for the standard model run can be seen in Fig. 7. Buoyancy flux convergences produced by salt fingering cause the perturbation to grow rapidly, and elevated values of R_ρ soon appear near the center of the model domain and at the edges. This results in decreased viscosities and increased vertical shears in these high-R_ρ regions as the fluid is more ''slippery.'' Eventually the intrusions become large enough in amplitude that salinity inversions appear; the fluid within these inversions is stably stratified in both heat and salt. As the evolution continues, advection of cooler water over warmer water causes temperature inversions to occur; the fluid within these inversions is diffusively stratified (cool and fresh above warm and salty). The diffusive layers grow in thickness by entraining fluid away from stable regions. Table 3 gives a detailed overview of the stages in the evolution of intrusions toward a steady state.

The appearance of stably and diffusively stratified layers can be understood by considering the evolution of the model fields in the (*S*, *T*) plane. Figure 8 illustrates the evolution of a warm and salty intrusion (labeled **A**), and a cool, fresh intrusion (labeled **B**). The heavy line represents the basic-state *T–S* curve, and vectors show the direction of evolution in *T–S* space, which is de-

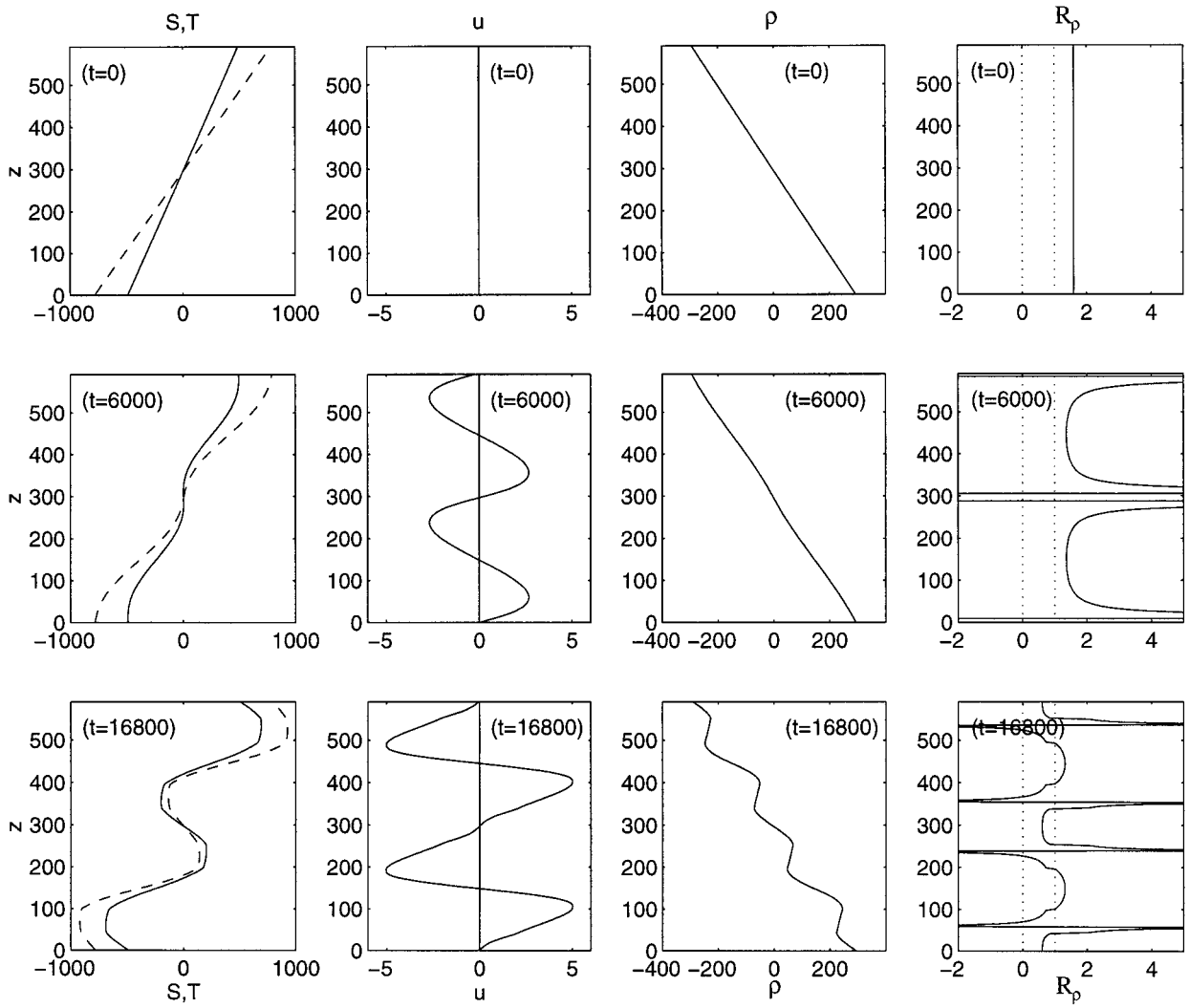

FIG. 7. Plots of S (solid line), T (dashed line), u, ρ, and R_ρ for the run shown in Fig. 4 at three different times: $t = 0$ (top row), $t = 6000$ (middle row), and $t = 16\,800$ (bottom row).

termined by a combination of advective and double-diffusive fluxes. Notice that the evolution is very nearly isopycnal, with warm/salty intrusions rising slightly relative to isopycnals. When intrusions grow sufficiently large that a salinity inversion occurs, the intervening fluid becomes stably stratified in both heat and salt (location 1). Eventually they grow to the point that a temperature inversion occurs between **A** and **B** (location 2), at which point the fluid between **A** and **B** is diffusively stratified.

TABLE 3. Stages of intrusion growth for the model run shown in Fig. 4. Times are given in nondimensional units, as well as in multiples of the linear e-folding period ($\approx$1115), and in terms of the buoyancy period $2\pi/N$.

Stage	t	Linear growth periods	Buoyancy periods	Comments
1	0–5900	0–5.3	0–940	Finger stratified everywhere Exponential growth even at ''large'' amplitude
2	5900	5.3	940	Salinity inversions appear Exponential growth continues
3	6400	5.7	1020	Temperature inversions appear
4	7100	6.4	1130	Density inversions appear Growth slows
5	12 000	10.8	1910	Steady state achieved

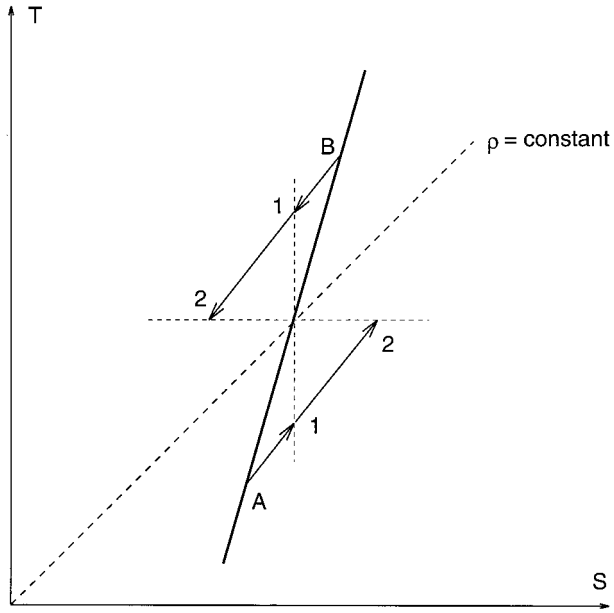

FIG. 8. Schematic illustration of the evolution of a typical model run in the (S, T) plane (adapted from McDougall 1986). The vectors show the evolution of a warm salty (rising) intrusion (**A**), and a cool fresh (descending) intrusion (**B**). As the intrusion grows, the overall stratification between **A** and **B** changes from being finger-sense to stable in both properties at point ''1,'' and eventually becomes diffusively unstable at point ''2.''

In Fig. 9 vertical profiles of the terms in the density and momentum equations are plotted. Figure 9a illustrates the imbalance between advective and diffusive fluxes that drives intrusion growth (panel 1), and the eventual equilibration of the fluxes (panel 6). While the intrusion amplitude is relatively small, double-diffusive flux divergences ($-F_{\rho,z}$, shown as solid lines) dominate over advective flux divergences ($u\overline{\rho}_x$, dashed lines) and accelerate the interleaving motions, but as t increases double-diffusive fluxes adjust relative to advective fluxes to allow equilibration. By $t = 9000$ the density field within the diffusive layer (at the center of the model domain) is close to a steady balance. The convecting layers are also nearly at equilibrium, as the destabilizing buoyancy fluxes into the layers are nearly balanced by the restratifying along-layer flows. The finger-stratified regions are still far from equilibrium, however, and are responsible for the continued evolution of the model fields. Figure 9b shows vertical profiles of the terms in the cross-front momentum equation. Note that the balance is close to a steady equilibrium (compared to the ρ equation) for the entire period (this is likely a result of the relatively large Prandtl number used in the run). There is, however, a slight imbalance between friction [$(Au_z)_z$] and buoyancy ($\tilde{\rho}\tan\theta$) that accelerates the flow. Once convection begins ($t = 7100$) the balance is almost perfect, as the drag exerted by the convecting layers on the flow within the finger-stratified layers decelerates the finger-layer flow dramatically. By $t = 18\,600$ the intrusions are very close to a steady equilibrium.

Convecting layers and entrainment

After diffusive layers have formed, quasi-isopycnal alonglayer advection drives R_ρ toward one in both the finger and diffusive regions (see Fig. 6). This is accompanied by increased vertical T–S fluxes, as T–S gradients become larger. There is also a persistent mismatch between the T–S flux ratio above and below the finger/diffusive interface, which—along with the heightened T–S fluxes—eventually produces a density inversion. Once a density overturn occurs, the resulting convecting layer grows rapidly by entraining fluid from adjacent layers. These convecting layers help to couple the diffusive- and finger-stratified layers, by fluxing excess buoyancy from finger- to diffusively stratified regions. In this way, they appear to play an important part in slowing the growth of intrusions, and in their eventual equilibration.

It can be shown (see the appendix) that the rate at which fluid is entrained into the convecting layers depends upon ''internal'' parameters (e.g., the height and amplitude of an overturn and the diffusivity K_{conv}), as well as on conditions outside the convecting layers (e.g., the ambient stratification). An interesting feature apparent in Fig. 5 is that convecting layers entrain fluid preferentially from finger-stratified layers, rather than diffusive layers. The reason for the preferential entrainment is not obvious, but it appears to be related to the different stratifications in the finger and diffusive regions. These different stratifications result from the fact that both advective and double-diffusive fluxes act to increase the stratification within diffusive layers, while at the edges of finger regions the combination of advective and double-diffusive fluxes acts to decrease the local stratification, so water from finger regions is more easily entrained. The equation governing the evolution of the density stratification is

$$\rho_{zt} = -u_z\overline{\rho}_x - F_{\rho,zz}, \tag{23}$$

which shows that the local density stratification can change due to either vertically sheared flow in a lateral density gradient or a divergent small-scale density flux.

In Fig. 10 the advective–diffusive balances in the finger and diffusive layers are shown schematically. The plot shows vertical profiles of u within the finger and diffusive regions for a growing intrusion. To investigate the effect of advective and double-diffusive fluxes on the stratification, consider the evolution of an intrusion in the (S_z, T_z) plane, starting with the point **a**, near the center of the finger region. The tendency of advection is to increase both S_z and T_z at **a**, destabilizing the water column, as shown by the vector labeled **adv**. However, double-diffusive fluxes decrease both S_z and T_z in such a way that the local stratification increases. Finger fluxes dominate in density terms, leading to an increase in the

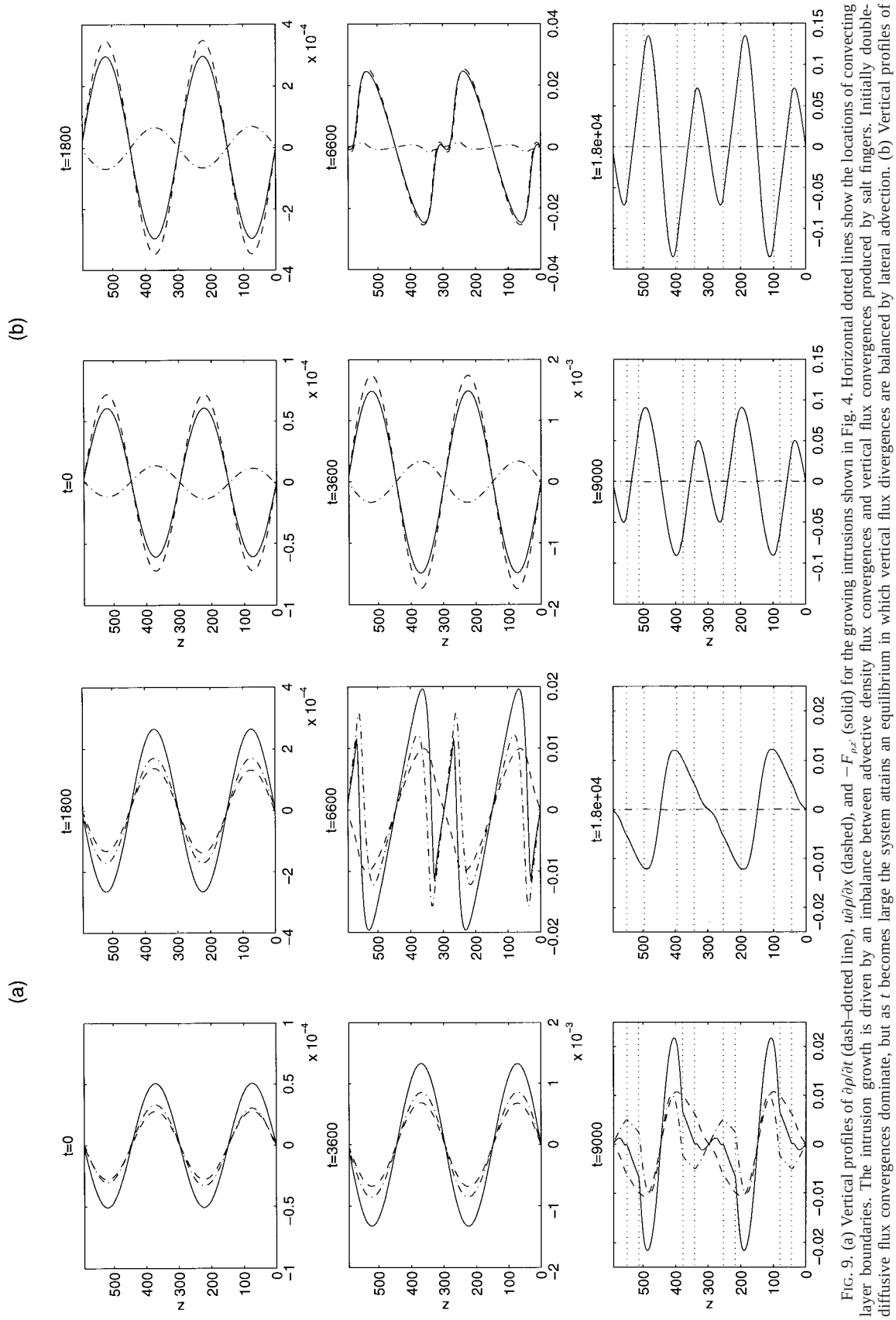

FIG. 9. (a) Vertical profiles of $\partial\rho/\partial t$ (dash–dotted line), $u\partial\rho/\partial x$ (dashed), and $-F_{\rho x'}$ (solid) for the growing intrusions shown in Fig. 4. Horizontal dotted lines show the locations of convecting layer boundaries. The intrusion growth is driven by an imbalance between advective density flux convergences and vertical flux convergences produced by salt fingers. Initially double-diffusive flux convergences dominate, but as t becomes large the system attains an equilibrium in which vertical flux divergences are balanced by lateral advection. (b) Vertical profiles of the terms in the momentum equation: $\partial u/\partial t$ (dash–dotted), $\rho' \tan\theta$ (dashed), and $(Au_z)_z$ (solid).

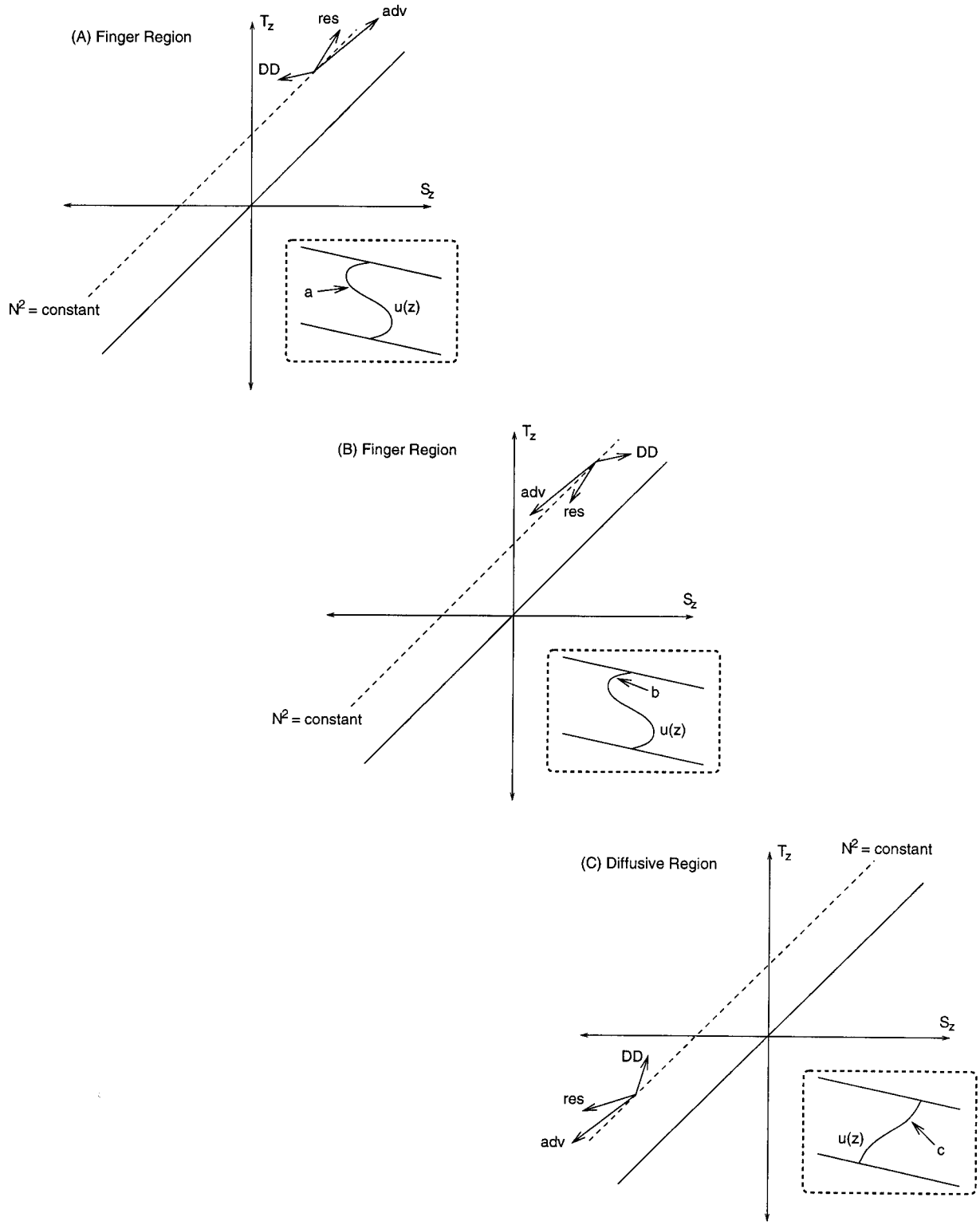

FIG. 10. Schematic showing the effect of advective and double-diffusive fluxes on the stratification in the finger and diffusive regions (at an intermediate stage in the growth of the intrusions). Near the center of the finger region (a) advection (labeled adv) tends to decrease the value of N^2, but finger fluxes (labeled DD) have a stabilizing tendency, and the combined fluxes (res) lead to an increase in the local value of N^2. Near the edges of the finger region the combination of advective and double-diffusive fluxes has a destabilizing effect on N^2 (b). In the diffusively stratified layer (c) both advective and double-diffusive fluxes have a stabilizing influence on the density stratification.

stratification at **a**. At point **b**, near the edge of the finger region, the roles of double-diffusion and advection are reversed. In this case advection tends to *increase* the stratification at **b**, as shown in Fig. 10b. However, finger fluxes dominate again, leading to a decrease in the stratification at **b**. Figure 10c shows the corresponding situation in the diffusive layer. In this case both advection and double diffusion lead to an increased stratification (suggesting a steady balance within the diffusive layer is not possible without additional vertical mixing processes). Therefore, small values of ρ_z at the edges of finger layers (relative to values at the edges of the diffusive layers) are a natural feature of intrusion evolution, and the likely explanation of the differential entrainment seen in Fig. 5.

4. Intrusion equilibration

As time increases the model solutions approach a steady state in which friction balances buoyancy forces and lateral advection of heat and salt is balanced by vertical flux divergences. At equilibrium the equations satisfied by u, S, and T are

$$\begin{aligned} \tan\theta(1 + S_{z'} - T_{z'}) &= [A(R_\rho)u_z]_{zz} \\ u_z\overline{S}_x &= [K_S(R_\rho)S_{z'}]_{zz} \\ u_z\overline{T}_x &= [K_T(R_\rho)T_{z'}]_{zz}, \end{aligned} \tag{24}$$

which is the steady version of the set (10). The approach to equilibrium can be shown graphically by plotting *T*–*S* tendency vectors, which are plotted in Fig. 11 for a warm, salty intrusion in the standard model run (the flux balances shown are averages over the depths between the centers of finger and diffusive layers). The top panel shows the situation before *T*–*S* inversions occur (so the water column is finger-stratified at all depths): the tendency of advection is to make the fluid within this depth range heavier, but the net double-diffusive flux into the layer overwhelms this tendency, so the intrusion becomes warmer, saltier, and lighter (as shown by the filled circle labeled res.). The bottom panel shows the situation at equilibrium: a diffusive layer has formed, and there is a three-way vector balance between diffusive fluxes in the top of the intrusion, finger fluxes through the bottom, and advective fluxes. In the remainder of this section we will discuss the factors that allow the interleaving solutions to approach the equilibrium apparent in panel b. We will first argue for the necessity of *T*–*S* overturns, which allow for a different flux ratio above and below an intrusion, and then for the necessity of flux ratio variations within each layer, which for our model solutions are brought about by turbulent mixing.

a. Are T–S inversions necessary for equilibration?

McDougall (1985b) has shown that *T*–*S* inversions are a necessary condition for the existence of equilibria

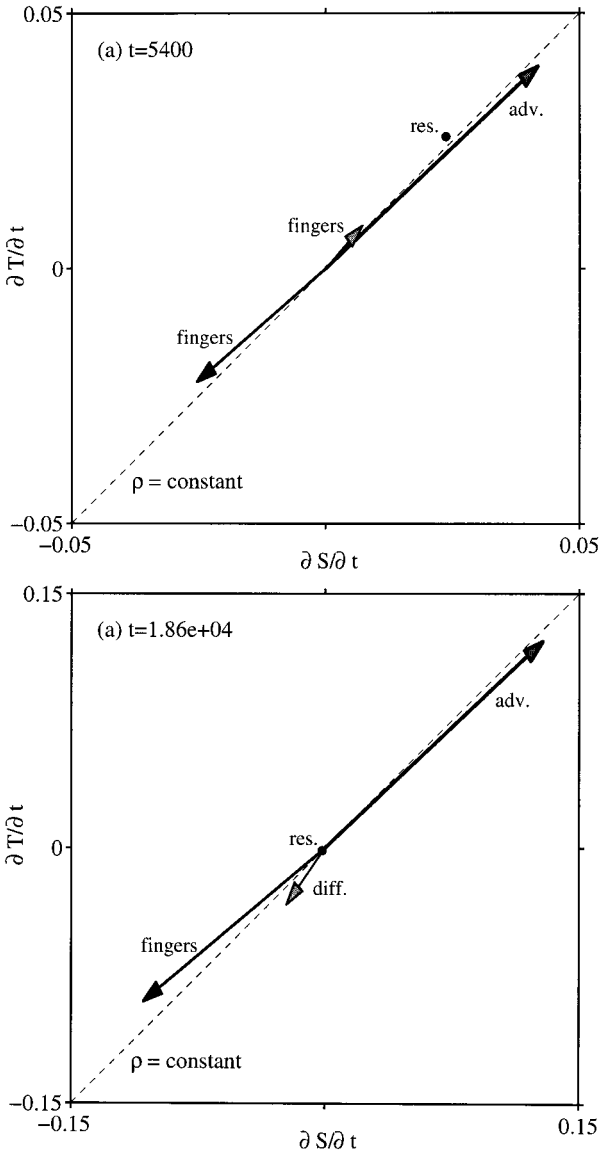

FIG. 11. The *T*–*S* flux balance for a warm and salty intrusion. At $t = 5400$ *T*–*S* inversions have not yet occurred, and the imbalance between double-diffusive and advective flux divergences makes the intrusion warmer, saltier, and lighter, and accelerates the flow. At equilibrium there is a three-way balance between advective, diffusive, and salt finger fluxes.

for his ''slab'' intrusion model. He did not consider the effect of turbulent mixing on intrusions, and it seems possible that strong turbulent mixing could prevent inversions from occurring by allowing for an inversion-free steady state. We will show that this is not so, using a straightforward extension of McDougall's argument. McDougall's argument is based on the idea that *T*–*S* equilibrium requires a balance between advective flux divergences and vertical double-diffusive *T*–*S* flux divergences. In the case he considered mixing processes were characterized by fixed, distinct *T*–*S* flux ratios, making it impossible to get a *T*–*S* flux balance without

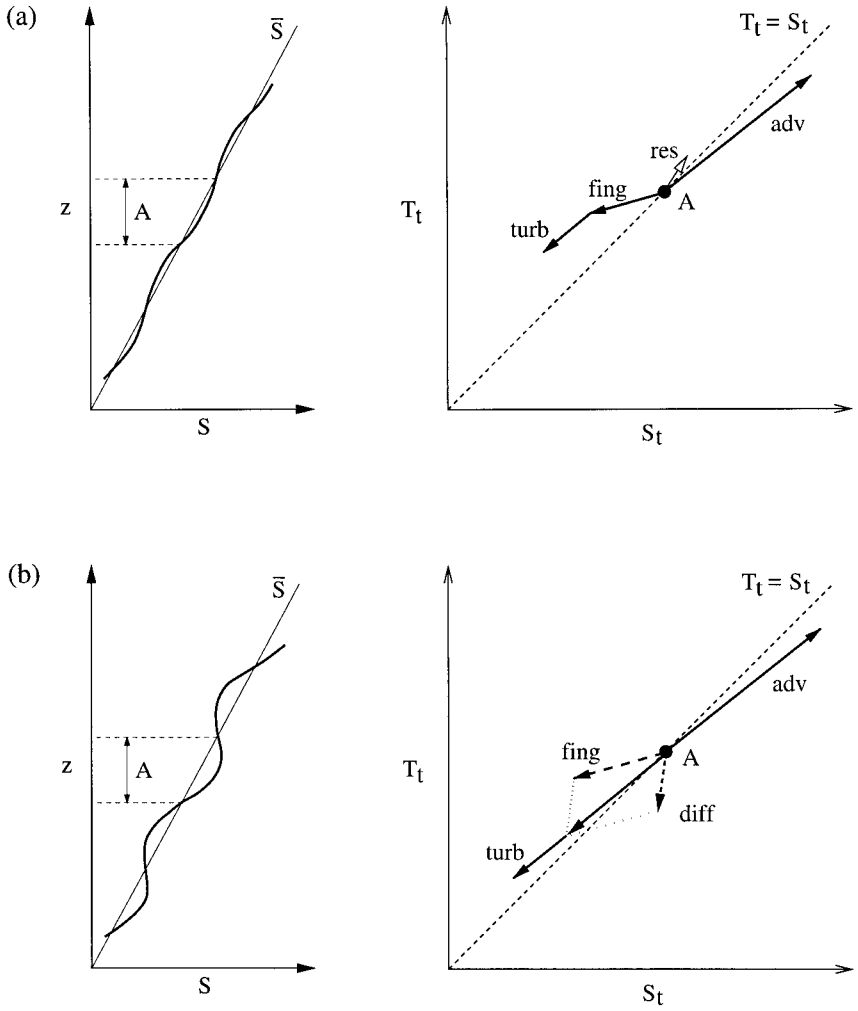

FIG. 12. Plot showing the bulk *T–S* flux divergences into the depth interval ''A'' occupied by a warm, salty (rising) intrusion. (a) The contributions of advection, salt fingering, turbulent mixing, and their resultant early in the intrusion life cycle (before inversions appear). Because the turbulent flux-divergence vector (labeled turb) is collinear with the advective flux-divergence vector (adv), turbulent mixing cannot bring about equilibration. (b) The situation after inversions appear, with the dashed arrows representing the fluxes in the top and bottom of the intrusion and the solid arrow the resulting flux-divergence vector. In this case a three-way vector balance between turbulence, double-diffusion, and advection is possible.

a diffusive interface (his argument was thus not for the necessity of overturns per se, but rather for the necessity of depth variations of the *T–S* flux ratio).

Now consider the situation in which both turbulence and double diffusion are active, shown schematically in Fig. 12. The depth-averaged balance between advective, double-diffusive, and turbulent *T–S* flux divergences is shown by vectors representing rates of change in *T* and *S*. The balances shown are for a warm and salty intrusion occupying the depth interval **A**, and the slopes of the vectors represent the ratio of *T–S* flux divergences for the various processes. To achieve an equilibrium the advective, double-diffusive, and turbulent flux-divergence vectors must sum to zero. Figure 12a shows the situation before inversions occur. The resultant of turbulent, double-diffusive, and advective flux divergences causes the warm and salty anomaly **A** to become less dense, and the resulting buoyancy forces produce an acceleration upward and across the front. The salt finger vector has a slope equal to the finger flux ratio γ_f ($\approx$0.6), while the slope of the advective vector is larger ($\approx$0.95 for the standard model run)—equal to that of the turbulent flux-divergence vector. The turbulent and advective flux-divergence vectors are collinear, since turbulence ''tries'' to remove the advective *T–S* disturbance and to restore the *T* and *S* profiles to their initial states. Because these vectors are not parallel with the salt finger flux-divergence vector, a three-way balance is not possible. However, after overturns occur (Fig. 12b), diffusive fluxes modify the net double-diffusive

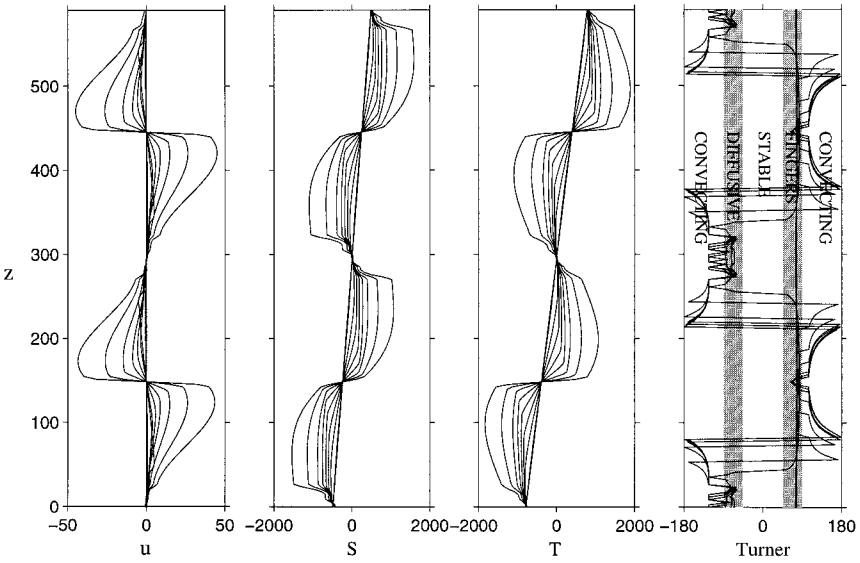

FIG. 13. Run showing the effect of using a small turbulent diffusivity K_{turb} ($K_{\text{turb}} = 0.001$). Profiles of u, S, T, and Turner angle are overplotted, showing the evolution of a small amplitude disturbance to to the point where interfaces are no longer resolved. Notice the ''steppy'' character of the T–S profiles within the diffusive region. The different curves correspond to successive times.

flux into an intrusion (shown as the resultant of the dashed finger and diffusive flux vectors), allowing a three-way balance between advection, double diffusion, and turbulence. Thus, McDougall's argument is changed little by the inclusion of turbulent mixing: with or without turbulence, it is impossible to achieve a balance between small-scale vertical fluxes and advection before T–S inversions occur.

b. What is the role of turbulent mixing?

To investigate the role that turbulent mixing plays in the equilibration process, we ran the model with extremely weak turbulent mixing ($K_{\text{turb}} = 0.001$). The model output (Fig. 13) shows that when K_{turb} is this small, convecting layers separated by extremely thin finger interfaces and ''steppy'' diffusive regions form as time proceeds. This run was stopped when the individual diffusive interfaces within the diffusive ''staircase'' became unresolved (i.e., thinner than the gridpoint spacing). A number of runs were done to check that the observed ''steppiness'' was not due to a numerical instability by varying Δz and Δt. The tests suggest that the staircase structure is a robust feature, which apparently results from the negative density diffusivity intrinsic to double diffusion. However, that staircaselike profiles are not observed to form as a result of the evolution of purely one-dimensional T–S disturbances using these flux laws (Walsh and Ruddick 1995b) suggests that the staircaselike features within the diffusive layers result from an interaction between advection and double-diffusive fluxes within intrusions.

Notice that if $K_{\text{turb}} = 0$, then (24b,c) and (14) imply that $\overline{T}_x/\overline{S}_x = \gamma_f$ in salt fingering regions. This condition cannot be satisfied, as it is inconsistent with exponential growth at small amplitude. The reason for this is that, if $K_{\text{turb}} = 0$, then γ_f must be less than $\overline{T}_x/\overline{S}_x$ during the linear growth stage so that warm, salty intrusions are made buoyant by finger fluxes [assuming a finger-favorable basic state; e.g., see Walsh and Ruddick (1995a)]. However, neither γ_f nor $\overline{T}_x/\overline{S}_x$ can evolve in time, which suggests a mechanism exists to allow one or both of these quantities to evolve as the intrusions grow. We assume that neither background gradients nor slopes change with time, which rules out changes in $\overline{T}_x/\overline{S}_x$. We will show that a nonzero K_{turb} permits the ratio of T and S flux *divergences* (or the ''flux-divergence ratio,'' denoted by γ_{div}) to evolve toward $\overline{T}_x/\overline{S}_x$, which allows growing intrusions to equilibrate. Interestingly, the superposition of turbulence and double diffusion in (14) gives a flux-divergence ratio different from the effective T–S flux ratio, and this has important implications for equilibration—this is why the distinction is made between the flux-divergence ratio and the flux ratio. Most previous interleaving studies have used a constant salt finger flux ratio, and have not incorporated the effects of turbulent mixing, in which case the flux ratio and the flux-divergence ratio are equal, making the distinction unnecessary.

The equilibrium flux condition can be derived by considering the flux balances through a small area in the finger region, as shown in Fig. 14. At equilibrium, vertical flux divergences must be balanced by lateral flux divergences. Linking the fluxes of heat and salt with an effective T–S flux ratio γ_{eff} and taking the ratio of the steady-state T and S conservation expressions gives

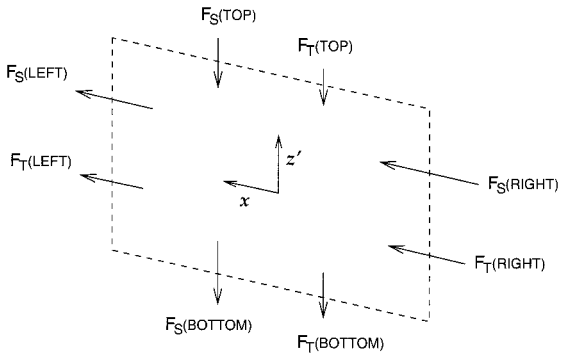

FIG. 14. Examination of the *T–S* fluxes (F_T, F_S) through a small area element within the finger-stratified region. Equating the vertical flux divergences through the box with the lateral advective flux divergences shows that the layer density ratio ($\overline{T}_x/\overline{S}_x$) must equal the flux-divergence ratio (γ_{div}) at equilibrium.

$$\frac{T^{(L)} - T^{(R)}}{S^{(L)} - S^{(R)}} = \frac{\gamma_{\text{eff}}^{(T)} + \gamma_{\text{eff}}^{(B)}}{2} + \frac{\gamma_{\text{eff}}^{(T)} - \gamma_{\text{eff}}^{(B)}}{h} \frac{(F_S^{(T)} + F_S^{(B)})/2}{(F_S^{(T)} - F_S^{(B)})/h}, \quad (25)$$

where h is the height of the area element, and F_S denotes the vertical salt flux due to a combination of turbulence and double-diffusion. The superscripts (*T*), (*B*), (*L*), and (*R*) refer to the top, bottom, left side, and right side of the elemental box, respectively. Letting $h \to 0$, we find that

$$\frac{T_x}{S_x} = \frac{\overline{T}_x}{\overline{S}_x} = \gamma_{\text{eff}} + \frac{\partial \gamma_{\text{eff}}}{\partial z'} \frac{F_S}{F_{S,z'}} \quad (26)$$

at equilibrium [which could also have been derived from (24b,c)]. Because the ratio of *T* and *S* flux divergences due to mixing must equal the ratio of advective *T* and *S* flux divergences ($\overline{T}_x/\overline{S}_x$) at equilibrium, it follows that the equilibrium condition (26) can be written equivalently as

$$\overline{T}_x/\overline{S}_x = F_{T,z'}/F_{S,z'} \equiv \gamma_{\text{div}}. \quad (27)$$

We will refer to $\overline{T}_x/\overline{S}_x$ as the ''layer density ratio,'' as it measures the ratio of *T–S* gradients along a layer. According to (26), depth variations of the flux ratio play an important role in the equilibration process. Within the context of this model, turbulent mixing is the only mechanism that can cause γ_{eff} to evolve within a layer. This can be seen from the definition of γ_{eff} [Eq. (22)], which shows that γ_{eff} is constant if $K_{\text{turb}} = 0$ but evolves with R_ρ if $K_{\text{turb}} \neq 0$, so variations in γ_{eff} are linked to variations in R_ρ through turbulence. This suggests that turbulence plays an important role in the equilibration of the model solutions.

The condition (26) allows an explanation for the piecewise-linear (S_z, T_z) profile, evident in Fig. 6b as the run approaches equilibrium. Straightforward manipulation of (26) gives

$$(\overline{T}_x/\overline{S}_x - \gamma_{\text{eff}})F_S = \text{const} \quad (28)$$

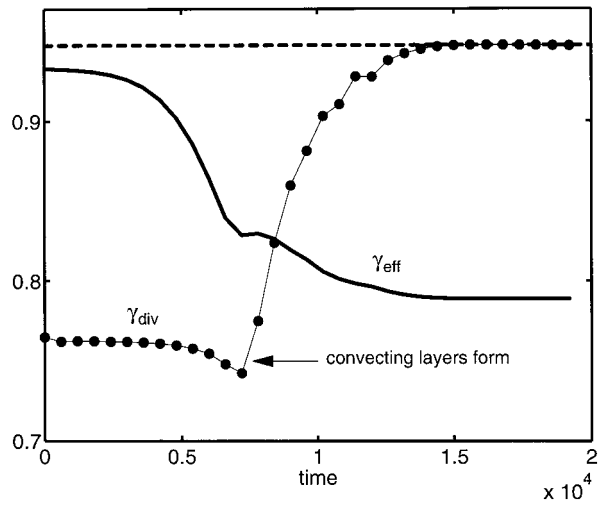

FIG. 15. Evolution of the effective flux ratio (γ_{eff}) and the ''flux divergence ratio'' γ_{div} for the run shown in Fig. 4, at a point within the finger-stratified region ($z \approx 184$). The layer density ratio $\overline{T}_x/\overline{S}_x$ is shown by the horizontal dashed line.

at equilibrium. Utilizing the definition of γ_{eff} (22) and using $F_S = -K_S S_{z'}$ shows that (28) describes a straight in the (S_z, T_z) plane if K_S is constant (as it is for the standard model run), although a nonconstant diffusivity would presumably introduce some curvature to the equilibrium (S_z, T_z) profiles.

It is informative to examine the terms in (26) as a model run approaches equilibrium. Figure 15 shows the time evolution of the flux divergence ratio (γ_{div}) and the effective flux ratio (γ_{eff}) near the center of the salt finger region ($z \approx 184$). The effective *T–S* flux ratio starts out close to 0.93 and decreases to a value of about 0.79 during the course of the run. Notice that the effective flux ratio is initially close to one, indicating that double-diffusive fluxes (with a flux ratio of 0.6) are strongly modified by turbulent *T–S* fluxes. The flux divergence ratio has a value of about 0.76 initially and remains relatively constant until $t \approx 7100$—at which time it increases rapidly to ~0.95 (the value of $\overline{T}_x/\overline{S}_x$)—the sudden increase coincides with the formation of the convecting layers seen in Fig. 4.

c. A run with diffusive stratification

In Fig. 16 a model run with diffusive-sense basic-state stratification is shown. We have not used the previously mentioned transformation suggested by Walsh and Ruddick (1995a) to find the fastest-growing disturbance for the diffusive case but have instead chosen the slope and domain height at random; the model fields ($\tilde{u}_z$, $\tilde{v}_z$, $\tilde{S}_z$, and $\tilde{T}_z$) were initialized with a white wavenumber spectrum, and the same slope was used for all wavenumber components. In spite of the different basic-state stratification and the fact that the run was not initialized with the fastest-growing disturbance, the model

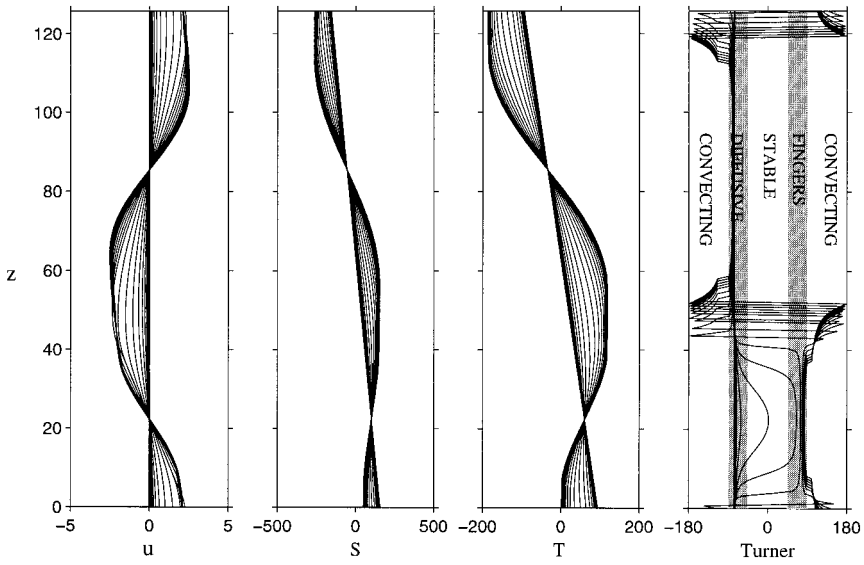

FIG. 16. A run with diffusive-sense basic-state stratification. Vertical profiles of *u, S, T,* and Turner angle are overplotted, showing the evolution of an infinitesimal disturbance to a large amplitude equilibrium. Different curves correspond to successive times.

fields evolve in much the same way as for the finger-stratified case and eventually achieve an equilibrium. By $t = 10\,000$ the run has equilibrated, with relatively thick diffusively stratified layers separated from thin finger-stratified layers by convecting layers. This shows that equilibration can be expected even when intrusion growth is driven by diffusive fluxes and suggests that equilibration is not specific to the fastest-growing disturbances but is likely to result from arbitrarily chosen initial conditions.

d. The role of nonconstant diffusivities

Ruddick (1984) investigated the evolution of an isolated thermohaline intrusion bounded above and below by diffusive and finger-sense interfaces, using a three-layer formulation. Ruddick's aim was to investigate formulations for the interfacial flux laws and to find conditions under which equilibrium solutions can exist without interfacial overturning. He considered the evolution of an isopycnal disturbance (advective effects were not considered), and found that the evolution of the system was sensitive to the form of the flux laws. In particular, if the overall stratification was finger favorable, steady intrusive solutions were possible only if the diffusive fluxes could dominate over the finger fluxes for some values of the interfacial density ratio. Ruddick concluded that the diffusive-sense diffusivity must increase more rapidly as $R_\rho \to 1$ than the finger-sense diffusivity to allow an equilibrium, apparently precluding steady solutions if double-diffusive diffusivities are constant.

To explore the consequences of specifying double-diffusive diffusivities that vary with R_ρ within a given stratification regime (e.g., finger, diffusive), we ran the standard model run again, this time with nonzero diffusivity exponents [$n_f = 2$, $n_d = 3$ in (14)], giving diffusivities similar to those used by Ruddick (1984). Notice from (14) that this parameter choice will change the average balance between turbulence and double diffusion since the basic-state diffusivity $K_S^F(\overline{R}_\rho)$ decreases by a factor of $\overline{R}_\rho^{-2}$. The initialization for the run was not changed from the standard run, so in this case the model was not initialized with the most unstable disturbance for the chosen parameters. We find that the intrusions reach an equilibrium state whether or not the finger and diffusive diffusivities vary with R_ρ. Vertical profiles of *u, S, T,* and Turner angle are shown in Fig. 17, with the system being close to equilibrium by $t = 24\,000$. As discussed in section 4b, depth-variation of the flux ratio is a necessary condition for equilibration, and Eq. (22) shows that this requires only that K_{turb} be nonzero—not that K_S be a function of R_ρ. This appears to be in conflict with Ruddick's (1984) results but it is, in fact, a consequence of an additional degree of freedom inherent in our model. For the stratified model used here, fluxes through a layer can adjust, even if the *T–S* jump across a layer remains fixed, because the layer thickness can change. Thus, equilibrium is possible even when double-diffusive diffusivities are constant.

In our discussion of nonconstant diffusivities, we have considered only the case in which double-diffusive diffusivities decrease away from $R_\rho = 1$. This is at odds with fluxes predicted using a critical Stern number criterion (Stern 1969), which have finger diffusivities increasing with R_ρ (Kunze 1987). However, we find that specifying a finger diffusivity with this R_ρ dependence leads to unbounded growth rates at the smallest scales

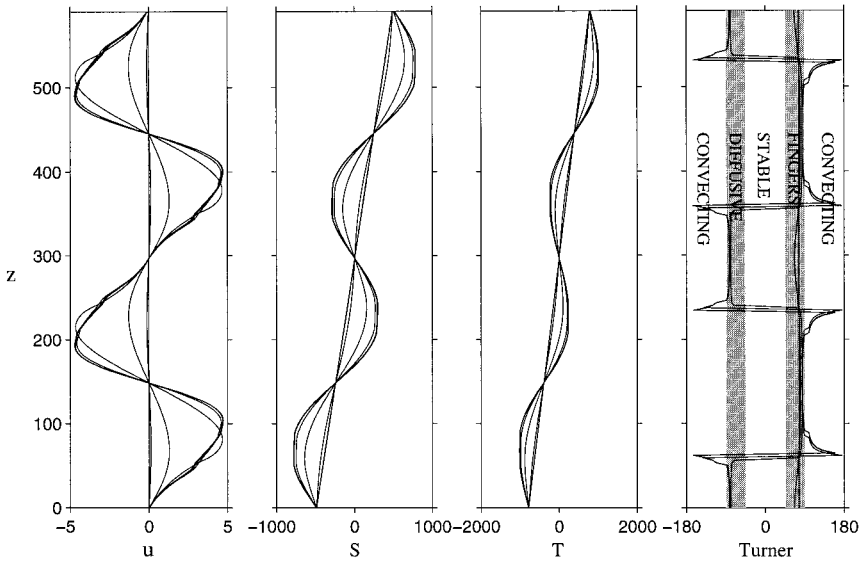

FIG. 17. A run in which the diffusivity exponents n_f and n_d are nonzero ($n_f = 2$, $n_d = 3$), so that diffusivities vary continuously with $\overline{R}_\rho$ in double-diffusively unstable conditions. All other parameters are identical to those for the run shown in Fig. 4. Vertical profiles of *u, S, T,* and Turner angle from successive times are overplotted, showing the evolution of a small amplitude disturbance to a large amplitude equilibrium.

(an ''ultraviolet catastrophe'') similar to the behavior discussed by Walsh and Ruddick (1995b).

To check that using Ruddick's (1985) viscosity parameterization (in which double-diffusive momentum fluxes are proportional to buoyancy fluxes) was not affecting the equilibration process in an unforeseen way, we ran the standard model run again using the alternate viscosity formulation in (14) (in which momentum fluxes are assumed to be proportional to salt fluxes) and found that the model was still able to achieve an equilibrium. Thus, while the size and functional form chosen for the viscosity doubtless affect the details of the final equilibrium that is reached (since at equilibrium there must be an average balance between the frictional forces retarding intrusions and buoyancy forces driving them), the qualitative picture is unchanged by the viscosity modification.

5. Discussion

McDougall (1985b) suggested that a three-way balance between finger, diffusive, and advective fluxes is necessary for growing intrusions to equilibrate—in essence a different flux ratio is required through the ''interfaces'' above and below slablike convecting layers in his model. McDougall did not, however, establish that such equilibria could, in fact, be reached—only that they are plausible. The model runs we have done verify that such equilibrium solutions are possible and that they can be attained via the evolution of small amplitude intrusions to large amplitude. The bulk flux balances across a convecting layer at equilibrium are similar to those described in McDougall (1985b) in that a three-way balance between finger, diffusive, and advective fluxes holds (Fig. 11). However, because we use a continuously stratified model rather than McDougall's ''slab'' representation, we must also consider the balances within individual finger and diffusive layers. Our results show that turbulent mixing is necessary to bring the finger and diffusively stratified layers into *internal* equilibrium.

The reason turbulence is essential to the equilibration of the model solutions is that it allows the ratio of T and S flux divergences due to mixing (γ_{div}) to evolve toward the layer density ratio ($\overline{T}_x/\overline{S}_x$) with time. Within our model framework turbulent mixing is the only process that can alter the flux ratio (for a particular stratification regime), although in reality other processes may also act to change the flux ratio. In particular, there is a fair amount of evidence suggesting that the double-diffusive flux ratios (γ_d, γ_f) are in fact functions of the density ratio. For example, Turner (1965) performed laboratory experiments that indicate that γ_d is constant for $R_\rho < 1/2$, but increases rather rapidly from 0.15 to 1.0 between $R_\rho = 1/2$ and $R_\rho = 1$. Kelley (1984) analyzed data from thermohaline staircases that seem to confirm that the diffusive flux ratio increases as R_ρ approaches 1. Stern's (1975) salt finger model predicts that the finger flux ratio should also be larger for R_ρ near 1. It is therefore conceivable that these variations, which are inherent to double-diffusive convection, could allow the flux ratio adjustment necessary for equilibration even in the absence of turbulence. Our decision to use a constant double-diffusive flux ratio in this work was motivated by a desire to keep the flux laws ''simple.''

The convecting layers apparent in our model runs are reminiscent of ''steps'' found by Zhurbas et al. (1987), who investigated the evolution of one-dimensional (isopycnal) *T*–*S* disturbances under the action of salt finger mixing. Zhurbas et al. found that, depending on the initial *T*–*S* stratification and the amplitude of the disturbance, the equilibrium solutions could have either a staircaselike character (i.e., relatively thin finger-stratified regions separated by well-mixed ''steps''), or they could achieve a steady state without steps. Interestingly, he found that for a given disturbance amplitude, solutions with steps occurred only for relatively small values of R_ρ. Equivalently, for a given R_ρ, only relatively large *T*–*S* disturbances (typically large enough to produce inversions in *T* and/or *S*) developed into solutions with steps. Our model is considerably more complex than that of Zhurbas et al., in that cross-frontal advection is an inherent part of the dynamics, and the maximum amplitude of the *T*–*S* disturbance cannot be prespecified (as in the work of Zhurbas et al.), but must be computed as part of the evolving solution. Nevertheless, the parallels between the two models are intriguing. The runs we have done suggest that infinitesimal disturbances frequently (if not always) become large enough that convecting layers form.

Our results suggest that intrusions can grow even when background turbulence is very intense compared with double diffusion. Model runs show that intrusions grow even in the case where turbulence is strong enough that γ_{eff} is initially everywhere larger than one (i.e., turbulence is strong enough to change the sign of the vertical buoyancy flux). From the available linear stability analyses (Toole and Georgi 1981; McDougall 1985a; Walsh and Ruddick 1995a), one might expect such a large *T*–*S* flux ratio to have a drastic effect on the character of the intrusions, making warm and salty parcels heavier rather than lighter, possibly changing the sign of the cross-front slope. However, our results show that even if γ_{eff} is initially everywhere greater than one, intrusions can grow as long as the flux-divergence ratio (γ_{div}) is less than one, and their slopes are unchanged by the strong turbulent mixing. Thus, γ_{div} is more fundamental to the intrusion dynamics than γ_{eff}, and (27), (26), and (22) show that γ_{div} and γ_{eff} are not equal if K_{turb} is nonzero.

Interestingly, the Froude number ($u_z = N_*^{-1}\partial u_*/\partial z_* \equiv \text{Fr}$) is supercritical ($>2$) across both the finger and the most pronounced of the diffusive interfaces for the run shown in Fig. 14 (in the latter stages of the run), suggesting that shear instabilities could occur at these locations in reality, leading to strong vertical mixing. The supercritical Froude numbers appear to be related to the weakness of turbulent mixing relative to double diffusion since the Froude number remained subcritical for the standard model run. Mixing coefficients in our model are insensitive to the value of the Froude number though, so fluxes do not change when Fr is supercritical. The high interfacial Froude numbers are reminiscent of observations made by Marmorino (1991) in the C-SALT thermohaline staircase. Marmorino found evidence of weak diffusive interfaces with high interfacial Froude numbers (between the strong salt-fingering interfaces) in the staircase.

6. Conclusions

We have developed a numerical model that simulates the evolution of thermohaline intrusions on a ''wide'' front in a computationally efficient manner, by assuming that the intrusions are one-dimensional (planar) disturbances with a fixed orientation. All model fields are assumed to be continuous in depth, and fluxes are specified using eddy diffusivities. In contrast with previous models of interleaving, mixing is assumed to be brought about by a linear superposition of turbulence and double-diffusive convection. Diffusivities are assumed to be functions of the density ratio (R_ρ), and are specified for all possible *T*–*S* stratifications (finger, diffusive, stable in *T* and *S*, and statically unstable). The model allows us to extend the linearized analytical studies of Toole and Georgi (1981) and others to the nonlinear regime.

Infinitesimal disturbances grow in accord with linear theory initially, and the linear growth stage seems qualitatively unchanged by the strong turbulent mixing that we use (with warm, salty intrusions still rising as they cross the front for a finger-favorable basic state). When the intrusion amplitude becomes large enough that *T*–*S* inversions occur, growth slows and the intrusions evolve toward an equilibrium state. The equilibria are characterized by layers of fluid with finger and diffusive-sense stratification separated by statically unstable ''convecting'' layers. Convecting layers facilitate the equilibration by allowing a large flux of buoyancy and momentum from finger to diffusively stratified layers.

Equilibration depends upon vertical variations of the turbulence-modified ''effective'' *T*–*S* flux ratio, γ_{eff}, both within a layer and from one layer to the next. Within the context of our model, turbulent mixing permits the necessary vertical variations in γ_{eff}, by allowing the effective flux ratio to evolve with R_ρ as intrusions grow. Hence, turbulence is essential to the equilibration of growing model solutions. At equilibrium, the layer density ratio $\overline{T}_x/\overline{S}_x$ is equal to the ''flux divergence ratio'' γ_{div}, which is not in general equal to the effective flux ratio γ_{eff}.

Solutions are found to be sensitive to the intensity of ''background'' turbulence, with weak turbulent mixing (small K_{turb}) leading to solutions with extremely thin finger interfaces and staircaselike structures within diffusively stratified regions. A larger value for K_{turb} gives solutions with thicker finger interfaces, and also eliminates the ''steppiness'' seen in diffusive regions for small values of K_{turb}. Specifying double-diffusive diffusivities that vary continuously with R_ρ has no apparent effect on the ability of the model solutions to equilibrate. The main effect of such nonconstant diffusivities ap-

pears to be a modification of the slope, wavenumber, and growth rate of the fastest-growing intrusion, as discussed by Walsh and Ruddick (1995a).

Acknowledgments. We wish to thank several people who provided feedback that helped improve this manuscript. Eric Kunze and George Veronis are especially acknowledged for giving valuable (and detailed) feedback on the manuscript. Victor Zhurbas and Natalia Kuz'mina also gave valuable comments on this work. We also wish to acknowledge useful discussions with Brian May.

APPENDIX

Evolution of a Density Overturn—Entrainment

Our parameterization scheme uses a large turbulent diffusivity—equal for heat, salt, and density—to rapidly mix those portions of the water column that are statically unstable. This differs from the explicit mixing scheme often used in general circulation models (Bryan and Cox 1968; Bryan 1969), which check for static instability and sequentially mix downward until static stability is achieved. Our scheme is slower than the direct mixing scheme but is symmetric in the vertical and diffusive in nature. When presented with a region of static instability bounded by stable regions, does the unstable region become homogeneous and entrain appropriately into the stable regions? To test this, we initialized the model with a purely thermal stratification consisting of a uniform stable gradient plus a finite-amplitude deviation, resulting in a region of static instability. The situation is shown schematically in Fig. A1, where a density inversion with initial thickness h_0 grows with time by entraining fluid from the surrounding stably stratified layers. The initial profile for the model runs and subsequent evolution of the density field is shown in Fig. A2a for $K_{conv} = 5$ in the unstable region and $K_{turb} = 0.01$ in the stable regions. It can be seen that the statically unstable region is rapidly homogenized while entraining the adjacent stable fluid until the water column reaches a marginally stable state. Note that the entrainment ceases when overall static stability is achieved, leaving only a minimal density jump between the mixed and stable region. The potential energy released by the buoyancy flux in the unstable region is just sufficient to entrain the stable fluid to the point of marginal stability, the remainder being lost to turbulent dissipation.

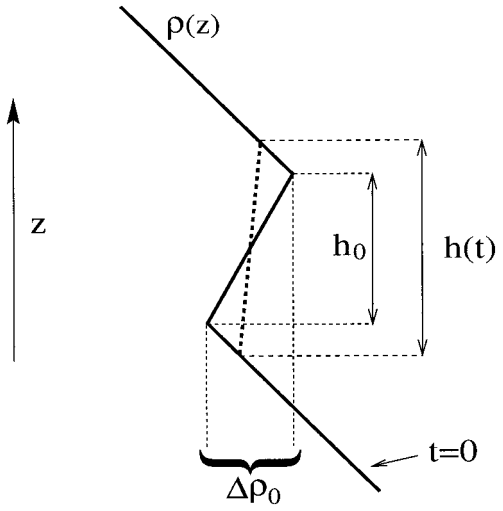

FIG. A1. Schematic of a localized density inversion in a stratified water column. The density profile at $t = 0$ is shown by the thick solid line; the profile at a later time is indicated by the thick dashed line. The overturn initially has vertical extent h_0 but grows thicker with time as the fluid adjusts and entrains fluid from the surrounding layers.

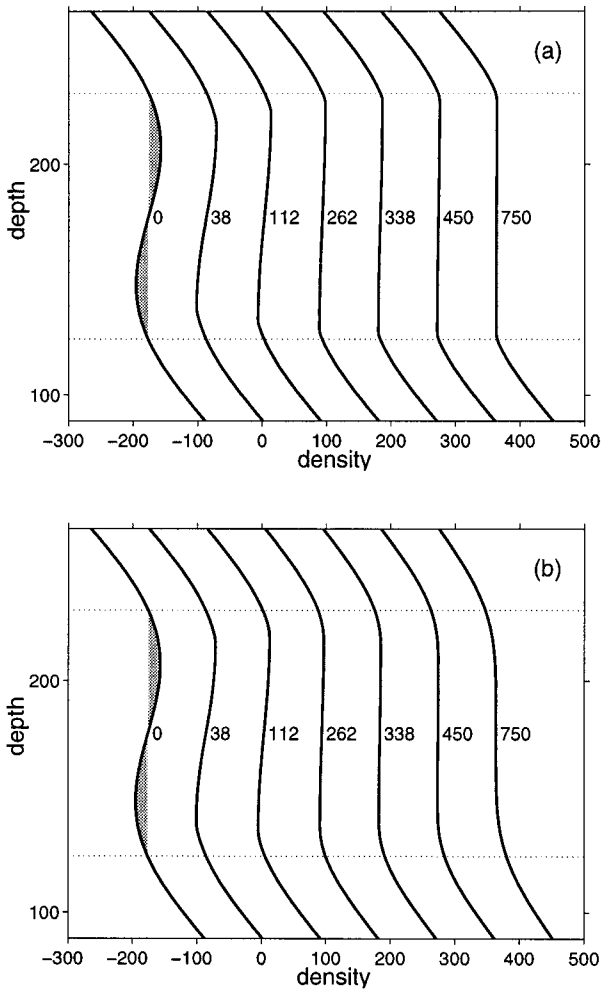

FIG. A2. Plots showing the evolution of an isolated density overturn for the case in which the entire water column is double-diffusively stable. The unstably stratified fluid adjusts rapidly, entraining into the stable water surrounding it. After the overturn disappears, the remaining homogeneous layer is eroded away from above and below by the less energetic mixing in stably stratified regions. In both (a) and (b) the diffusivity in the overturning region is $K_{conv} = 5$, while the low-level turbulent mixing in stably stratified regions is characterized by a diffusivity $K_{turb} = 0.01$ in (a) and by $K_{turb} = 0.3$ in (b).

This mirrors the development of a mixed layer in stratified fluid under penetrative convection in which the density jump between the mixed and stratified regions is observed to be small [Deardorff et al. (1969)—see Fig. 7.17 in Turner (1973)]. As discussed by Turner (1973, sections 7.3 and 9.2), the energy supplied by buoyant forcing is used to change the potential energy of the water column by mixing it with the fluid above, and sufficient dissipation occurs to prevent much entrainment of fluid beyond the level required to achieve static stability.

The time required for mixing within the unstable region is roughly $\tau_{\text{mix}} = h_0^2/K_{\text{conv}} = 720$, where $h_0 = 60$ is the initial height of the unstable region. There is, however, a second relevant timescale, based on the rate at which the unstable patch entrains water from the adjacent stable regions. Assuming that the density profile within the overturn remains approximately linear and that the surrounding stable layers have uniform stratification $\overline{\rho}_z$, it can be shown that the convecting layer will grow in thickness by ''entraining'' fluid from adjacent layers with entrainment velocity w_e, such that

$$\frac{dh}{dt} \equiv 2w_e = 8\left(\frac{K_{\text{conv}}/h(t) - K_{\text{turb}}\overline{\rho}_z/\Delta\rho(t)}{1 - h(t)\overline{\rho}_z/\Delta\rho(t)}\right), \quad \text{(A1)}$$

and that the eventual scale of the mixed fluid patch will be

$$h(t \to \infty) \approx \left(\frac{h_0 - \Delta\rho_0/\overline{\rho}_z}{1 - K_{\text{turb}}/K_\rho}\right), \quad \text{(A2)}$$

where the subscript 0 denotes the value of a quantity at time $t = 0$. These allow the entrainment timescale to be estimated as

$$\tau_E \equiv \frac{1}{2}\frac{h_\infty - h_0}{w_{e,0}} = -\frac{1}{8}\left(\frac{1 - h_0\overline{\rho}_z/\Delta\rho_0}{1 - K_{\text{turb}}/K_{\text{conv}}}\right)\frac{h_0\Delta\rho_0}{K_{\text{conv}}\overline{\rho}_z}. \quad \text{(A3)}$$

For the runs in Fig. A2 this has a value of about 150, so the entrainment timescale is much shorter than the ''internal'' mixing timescale. This may explain why the mixing seems to be essentially complete well before $t = 720$. As the mixing proceeds, the stable region diffuses at the slower rate K_{turb}, leaving a profile with relatively sharp ''corners.'' Figure A2b shows the same experiment with $K_{\text{turb}} = 0.3$, in which the diffusion within the stable regions results in much smoother profiles.

REFERENCES

Armi, L., D. Hebert, N. Oakey, J. Price, P. L. Richardson, T. Rossby, and B. Ruddick, 1989: Two years in the life of a Mediterranean Salt Lens. *J. Phys. Oceanogr.,* **19,** 354–370.

Barton, E. D., and P. Hughes, 1982: Variability of water mass interleaving off N.W. Africa, *J. Mar. Res.,* **40,** 963–984.

Bormans, M., 1992: Effect of R_ρ on double diffusive interleaving. *Deep-Sea Res.,* **39**(5), 871–884.

Bryan, K., 1969: A numerical method for the study of the circulation of the world ocean. *J. Comput. Phys.,* **4,** 347–376.

——, and M. Cox, 1968: A nonlinear model of an ocean driven by wind and differential heating. Part I: Description of the three dimensional velocity and density field. *J. Atmos. Sci.,* **25,** 945–967.

Bryden, H. L., 1979: Poleward heat flux and conversion of available potential energy in Drake Passage. *J. Mar. Res.,* **37,** 1–22.

Carmack, E. C., K. Agaard, J. H. Swift, R. G. Perkin, F. A. McLaughlin, R. W. MacDonald, and E. P. Jones, 1995: Thermohaline transitions. *Physical Limnology,* J. Imberger, Ed., IUTAM.

Chereskin, T., 1995: Direct evidence for an Ekman balance in the California Current. *J. Geophys. Res.,* **100,** 18 261–18 269.

Crapper, P. F., 1976: The transport across a density interface in the presence of externally imposed turbulence. *J. Phys. Oceanogr.,* **6,** 982–984.

Deardorff, J. W., G. E. Willis, and D. K. Lilly, 1969: Laboratory investigation of non-steady penetrative convection. *J. Fluid Mech.,* **35,** 7–31.

Garrett, C., 1982: On the parameterization of diapycnal fluxes due to double-diffusive intrusions. *J. Phys. Oceanogr.,* **12,** 952–959.

Holyer, J. Y., 1983: Double-diffusive interleaving due to horizontal gradients. *J. Fluid Mech.,* **137,** 347–362.

Horne, E. P. W., 1978: Interleaving at the subsurface front in the slope water off Nova Scotia. *J. Geophys. Res.,* **83,** 3659–3671.

Joyce, T. M., 1977: A note on the lateral mixing of water masses. *J. Phys. Oceanogr.,* **7,** 626–629.

——, W. Zenk, and J. M. Toole, 1978: The anatomy of the Antarctic polar front in the Drake Passage. *J. Geophys. Res.,* **83,** 6093–6113.

Kelley, D., 1984: Effective diffusivities within oceanic thermohaline staircases. *J. Geophys. Res.,* **89,** 10 484–10 488.

Kerr, O. S., 1992: Two-dimensional instabilities of steady double-diffusive interleaving. *J. Fluid Mech.,* **242,** 99–116.

Kunze, E., 1987: Limits on growing, finite-length salt fingers: A Richardson number constraint. *J. Mar. Res.,* **45,** 533–556.

——, 1994: A proposed flux constraint for salt fingers in shear. *J. Mar. Res.,* **52,** 999–1016.

Ledwell, J. R., and A. J. Watson, 1994: North Atlantic Tracer Release Experiment—Newest results. *WOCE Notes* (unpublished manuscript), **6** (1), 1–4.

——, A. J. Watson, and C. S. Law, 1993: Evidence for slow mixing across the pycnocline from an open-ocean tracer-release experiment. *Nature,* **364,** 701–703.

Linden, P., 1971: Salt-fingers in the presence of grid-generated turbulence. *J. Fluid Mech.,* **49,** 611–624.

Marmorino, G. O., 1991: Intrusions and diffusive interfaces in a salt-finger staircase. *Deep-Sea Res.,* **38,** 1431–1454.

May, B. D., and D. E. Kelley, 1997: Effect of baroclinicity on double-diffusive interleaving. *J. Phys. Oceanogr,* **27,** 1997–2008.

McDougall, T. J., 1985a: Double-diffusive interleaving. Part I: Linear stability analysis. *J. Phys. Oceanogr.,* **15,** 1532–1541.

——, 1985b: Double-diffusive interleaving. Part II: Finite amplitude, steady state interleaving. *J. Phys. Oceanogr.,* **15,** 1542–1556.

Morse and Feshback, 1953: *Methods of Theoretical Physics.* Int. Ser. Pure and Applied Physics, McGraw-Hill, 1978 pp.

Niino, H., 1986: A linear stability theory of double-diffusive horizontal intrusions in a temperature-salinity front. *J. Fluid Mech.,* **171,** 71–100.

Posmentier, E. S., and R. W. Houghton, 1978: Fine structure instabilities induced by double diffusion in the shelf/slope water front. *J. Geophys. Res.,* **83,** 5135–5138.

——, and A. D. Kirwan, 1985: The role of double-diffusive interleaving in mesoscale dynamices: A hypothesis. *J. Mar. Res.,* **43,** 541–552.

Press, W. H., B. P. Flannery, S. A. Teukolsky, and W. T. Vetterling, 1986: *Numerical Recipes: The Art of Scientific Computing.* Cambridge University Press, 818 pp.

Provost, C., and S. Gana, 1995: Hydrographic conditions in the Brazil–Malvinas confluence during austral summer 1990. *J. Geophys. Res.,* **100,** 10 655–10 678.

Richards, K. J., and R. T. Pollard, 1991: Structure of the upper ocean in the western equatorial Pacific. *Nature,* **350,** 48–50.

Ruddick, B. R., 1983: A practical indicator of the stability of the water column to double-diffusive activity. *Deep-Sea Res.,* **30,** 1105–1107.
——, 1984: The life of a thermohaline intrusion. *J. Mar. Res.,* **42,** 831–852.
——, 1985: Momentum transport in thermohaline staircases. *J. Geophys. Res.,* **90,** 895–902.
——, 1992: Intrusive mixing in a Mediterranean salt lens—Intrusion slopes and dynamical mechanism. *J. Phys. Oceanogr.,* **22,** 1274–1285.
——, and J. S. Turner, 1979: The vertical length scale of double-diffusive intrusions. *Deep-Sea Res.,* **26,** 903–913.
——, and D. Hebert, 1988: The mixing of Meddy ''Sharon.'' *Small-Scale Mixing in the Ocean,* J. C. J. Nihoul and B. M. Jamart, Eds., Elsevier Oceanogr. Ser., Vol. 46.
Schmitt, R. W., 1979: Flux measurements on salt fingers at an interface. *J. Mar. Res.,* **37,** 419–436.
——, 1981: Form of the temperature–salinity relationship in the central water: Evidence for double-diffusive mixing. *J. Phys. Oceanogr.,* **11,** 1015–1026.
Stern, M. E., 1967: Lateral mixing of water masses. *Deep-Sea Res.,* **14,** 747–753.
——, 1969: Collective instability of salt fingers. *J. Fluid Mech.,* **35,** 209–218.
——, 1975: *Ocean Circulation Physics.* Academic Press, 191–203.
Stommel, H., and N. K. Fedorov, 1967: Small scale structure in temperature and salinity near Timor and Mindinao. *Tellus,* **19,** 306–325.
Toole, J. M., 1981: Intrusion characteristics in the Antarctic polar front. *J. Phys. Oceanogr.,* **11,** 780–793.
——, and D. T. Georgi, 1981: On the dynamics and effects of double-diffusively driven intrusion. *Progress in Oceanography,* Vol. 10, Pergamon Press, 121–145.
Turner, J. S., 1965: The coupled turbulent transports of salt and heat across a sharp density interface. *Int. J. Heat Mass.,* **8,** 759–767.
——, 1973: *Buoyancy Effects in Fluids.* Cambridge University Press, 368 pp.
Walsh, D., and B. R. Ruddick, 1995a: Double-diffusively driven intrusions: The influence of non-constant diffusivities. *J. Phys. Oceanogr.,* **25,** 348–358.
——, and ——, 1995b: An investigation of Kunze's salt finger flux laws—Are they stable? *Double-Diffusive Convection, Geophys. Monogr.,* No. 94, Amer. Geophys. Union, 334 pp.
Washburn, L., and C. H. Gibson, 1984: Horizontal variability of temperature microstructure at the base of a mixed layer during MILE. *J. Geophys. Res.,* **89** (C3), 3507–3522.
Yoshida, J., H. Nagashima, and H. Niino, 1989: The behavior of a double-diffusive intrusion in a rotating system. *J. Geophys. Res.,* **94,** 4923–4937.
Zhurbas, V. M., N. P. Kuz'mina, and O. Y. E. Kul'sha, 1987: Step-like stratification of the ocean thermocline resulting from transformations associated with thermohaline salt finger intrusions (numerical experiment). *Oceanology,* **27**(3), 277–281.